UNIVERSITY OF CALIFORNIA
RIVERSIDE

Enhanced Situational Awareness in Power Distribution Systems: Data-Driven Analysis of Harmonic Synchro-Phasors and Synchro-Waveforms

A Dissertation submitted in partial satisfaction
of the requirements for the degree of

Doctor of Philosophy

in

Electrical Engineering

by

Fatemeh Ahmadi Gorjayi

September 2024

Dissertation Committee:

Dr. Hamed Mohsenian-Rad, Chairperson
Dr. Matthew Barth
Dr. Basak Guler

The Dissertation of Fatemeh Ahmadi Gorjayi is approved:

Committee Chairperson

University of California, Riverside

Acknowledgments

I would like to extend my deepest gratitude to my advisor, Prof. Hamed Mohsenian-Rad, for his help, support, and encouragement during my journey towards earning my PhD degree. His expertise, and insightful feedback provided invaluable opportunities for learning and growth.

Special thanks to Dr. Matthew Barth and Dr. Basak Guler, who graciously accepted the role of serving on my dissertation defense committee.

My heartfelt thanks go to my beloved husband, Alireza, who has stood by me through all the challenges of this journey. He has been not just a partner but also a mentor. His love, support, and encouragement are the true reasons for my success. Additionally, I extend my gratitude to my dear parents and my lovely siblings, for their endless support.

I am deeply grateful to my labmates in Smart Grid Laboratory for their friendship, encouragement, and support. Their collaboration and camaraderie have made the research process both enjoyable and fulfilling.

The content of this thesis is primarily based on the material that appeared in the first four publications listed below. Additionally, I have included references to other collaborative papers that I engaged in during my Ph.D. studies.

1. **Fatemeh Ahmadi Gorjayi**, and Hamed Mohsenian-Rad. "Physics-aware sparse harmonic state estimation in power distribution systems." *in Proc. 2022 IEEE Power & Energy Society Innovative Smart Grid Technologies Conference (ISGT)*, New Orleans, LA, April 2022.

2. **Fatemeh Ahmadi-Gorjayi** and Hamed Mohsenian-Rad. "A Physics-Aware MIQP Approach to Harmonic State Estimation in Low-Observable Power Distribution Systems Using Harmonic Phasor Measurement Units." IEEE Transactions on Smart Grid, vol. 14, no. 3, p.p. 2111-2124, May, 2022.

3. **Fatemeh Ahmadi-Gorjayi** and Hamed Mohsenian-Rad. "Data-Driven Models for Sub-Cycle Dynamic Response of Inverter-Based Resources Using WMU Measurements." IEEE Transactions on Smart Grid, vol. 14, no. 4, p.p. 4125- 4128, September, 2023.

4. **Fatemeh Ahmadi-Gorjayi**, Lutz Lampe, and Hamed Mohsenian-Rad, "Event Signatures in H-PMU Measurements: An Information-Theoretic Analysis of Real-World Data," *in Proc. 2024 IEEE Power & Energy Society Innovative Smart Grid Technologies Conference (ISGT)*, Washington, DC, February 2024.

5. Narges Ehsani, **Fatemeh Ahmadi-Gorjayi**, Zong-Jhen Ye, Alex McEachern, and Hamed Mohsenian-Rad, "Sub-cycle Event Detection and Characterization in Continuous Streaming of Synchro-waveforms: An Experiment Based on GridSweep Measurements," *in Proc. 2023 IEEE North American Power Symposium*, Asheville, NC, October 2023.

6. Hossein Mohsenzadeh-Yazdi, **Fatemeh Ahmadi-Gorjayi**, and Hamed Mohsenian-Rad, "Sub-Cycle Dynamics Modeling of IBRs Using LSTM Methods and Synchro-waveform Measurements," *in Proc. of the IEEE PES General Meeting*, Seattle, WA, July 2024.

To my beloved Alireza, Maman, and Baba.

ABSTRACT OF THE DISSERTATION

Enhanced Situational Awareness in Power Distribution Systems: Data-Driven Analysis of Harmonic Synchro-Phasors and Synchro-Waveforms

by

Fatemeh Ahmadi Gorjayi

Doctor of Philosophy, Graduate Program in Electrical Engineering
University of California, Riverside, September 2024
Dr. Hamed Mohsenian-Rad, Chairperson

Harmonic Phasor Measurement Units (H-PMUs) and Waveform Measurement Units (WMUs) are two emerging smart grid sensor technologies that are critical for enhancing situational awareness in power distribution systems and distributed inverter-based resources (IBRs), especially in the era of increased reliance on renewable energy resources and advanced grid edge technologies.

H-PMUs can particularly assist power system operators to enhance reliability in monitoring harmonic distortions, which have become more prevalent due to the growing number of power electronic devices and inverter-based energy resources. Harmonic State Estimation (HSE) plays a key role in developing real-time monitoring systems to help power distribution system operators identify harmonic sources and track their propagation. However, the limited deployment of power quality sensors in real-world power system presents a significant challenge.

To tackle this open problem, this thesis develops novel physics-aware HSE methods that leverage the radial topology of power distribution systems to identify sparsity pat-

terns. The two proposed approaches are: a Physics-Aware Sparse HSE using constrained weighted-Lasso optimization for single harmonic sources, and a Physics-Aware Mixed Integer Quadratic Program (MIQP) to estimate the number and locations of multiple harmonic sources without prior information.

Additionally, this thesis examines the information content in harmonic phasor signatures from power system events. Using real-world H-PMU measurements, we demonstrate that harmonic phasors can reveal new information content about power system events that are not captured by fundamental phasors from conventional PMUs. The proposed data-driven, information-theoretic approach enhances event clustering, particularly for transient and high-frequency events.

Furthermore, this thesis addresses the challenges due to the increasing deployment of Distributed Energy Resources (DERs) and their impact on the dynamic behavior of power systems, often occurring within fractions of a cycle. Utilizing real-world data from WMUs, novel data-driven methods were proposed to model the dynamic response of IBRs to high-frequency disturbances. These methods operate in both frequency domain, such as using modal analysis techniques, and in time domain, employing regression techniques such as finite impulse response and auto-regressive eXogenous models, to estimate IBRs' responses to high-frequency disturbances.

Contents

List of Figures

List of Tables

Chapter 1

Introduction

1.1 Background

The power systems consist of four main sectors: generation, transmission, distribution, and consumption. It facilitates the delivery of electricity from generators to consumers through transmission and distribution systems [1]. Electricity is predominantly transmitted in the form of alternating current (AC), characterized by sinusoidal variations in voltage and current over time.

Modern power systems face increasing complexities due to several factors. The integration of renewable energy sources, such as solar and wind power, has seen substantial growth to mitigate environmental impacts and reduce reliance on fossil fuels. However, these energy sources introduce various challenges to the power grid. For instance, power electronic devices, such as inverters and converters, play a pivotal role in integrating renewable energy sources into the grid and enhancing energy efficiency. However, these devices introduce harmonic and inter-harmonic distortions and non-linearities that can compromise

the quality and stability of power supply [2]. Furthermore, intermittent renewable generation and volatile loads inject significant uncertainty into system operations, potentially jeopardizing stability and security [3, 4, 5]. Moreover, the inertia-less nature of renewable generators adds to the challenges of maintaining power system stability [6].

Also, the introduction of new electrified technologies, such as plug-in electric vehicles, has contributed to a more varied load profile [7]. As EV adoption increases, so does the demand for electricity, particularly during peak charging hours. This not only affects the overall load on the grid but also introduces variability and unpredictability in demand patterns [8].

In addition to these technological shifts, the power system is increasingly exposed to extreme weather conditions, such as wildfires, hurricanes, and heatwaves, which pose significant threats to its infrastructure [9, 10]. Wildfires, for instance, can damage transmission lines, substations, and other critical components of the grid, leading to widespread power outages and interruptions in electricity supply.

In this regards, the increasing complexity and dynamic behavior of modern power systems, driven by the diversification of loads, the rapid deployment of power electronic devices, the integration of renewable energy sources, and also the impact of extreme weather events, underscore the need for enhanced real-time monitoring and situational awareness. Advanced smart grid sensors, such as Harmonic Phasor Measurement Units (H-PMUs) and Waveform Measurement Units (WMUs), offer the potential to address these challenges by providing high-resolution data and insights into the operational status of the power grid. This background sets the stage for exploring innovative methods to improve the reliability

and security of power distribution systems, especially in the context of low-observable grids. The following section will delve into the motivation behind this research, highlighting the necessity of utilizing these advanced sensor technologies to enhance the grid's resilience and performance.

1.2 Motivation

The evolution of the power system into a *smart* grid, incorporating advanced measurement technologies, is essential to address the myriad challenges facing modern power distribution systems [11]. As these challenges increase, so does the necessity for innovative approaches to monitoring and analysis that can fully utilize the capabilities of these new sensors. This section highlights the need for smart grid sensors and the difficulties posed by the limited availability of these devices, which result in low-observability in power distribution systems.

The first critical step in modernizing the power grid is the integration of cutting-edge technologies, such as smart grid sensors, which provide significant benefits for real-time monitoring and situational awareness. These sensors offer valuable insights into the operational status of the grid and its components. The three main classes of smart grid sensor technologies available for power distribution systems are: 1) Supervisory Control and Data Acquisition (SCADA) systems [12], 2) Phasor Measurement Units (PMUs), including harmonic phasor measurement units, and 3) Waveform measurement units.

SCADA systems have been widely integrated into distribution systems over the past fifty years [13]. They report the root-mean-square (RMS) representation of voltage

and current measurements and operate at low reporting rates, typically one sample per second. While SCADA systems have played a crucial role in monitoring, their capabilities are limited by their low resolution and reporting rate.

Over the past two decades, PMUs have been deployed in distribution systems to provide time-synchronized phasor measurements of voltage and current. Equipped with GPS, PMUs operate at high reporting rates, such as 120 samples per second (2 samples per AC cycle), offering significant advancements in monitoring and situational awareness [14]. Additionally, H-PMUs provide *harmonic* voltage and current phasor measurements, significantly enhancing the ability to monitor harmonic distortions in power systems [15, 16, 17, 18, 19]. However, phasor measurements also have limitations, particularly when voltage and current waveforms include distortions or non-sinusoidal shapes, which are increasingly common in modern grids [20].

WMUs represent the latest advancement in smart grid sensor technology, emerging to address the limitations of SCADA and phasor measurement units. WMUs capture the actual voltage and current waveforms in the time domain with extremely high reporting rates, such as 15,360 samples per second (256 samples per AC cycle). This high resolution allows WMUs to record detailed wave-shapes of voltage and current, enabling precise monitoring of transient and high-frequency events. WMUs provide high-resolution monitoring of inverter-based resources (IBRs) during rapid, sub-cycle disturbances, but the vast data they generate poses challenges for storage and processing.

Despite the significant benefits of smart grid sensors, their limited deployment in power distribution systems leads to low-observability. [21, 22, 23].

The limited availability of smart grid sensors in power distribution systems significantly hinders the ability to achieve harmonic state estimation (HSE). Although extensive research has been conducted on HSE at the transmission level, studies at the distribution level remain scarce [24]. This disparity primarily arises from the fundamental differences between power transmission and distribution systems. These differences include system balance [25], resistance-to-reactance ratio [26], lack of full-observability [27], and the uncertainties introduced by the high penetration of renewable energy resources [28, 29]. Because of these distinctions, the direct application of transmission system state estimation methods to distribution systems is often ineffective. These challenges are addressed in greater detail in Chapters 2 and 3.

Also, observability at the fundamental frequency can be achieved using different types of sensors like PMUs or smart meters. However, there are only a few sensors available for studying HSE. Therefore, a power distribution system could be fully-observable at the fundamental frequency while remaining low-observable at harmonic frequencies. This raises the question of how to achieve situational awareness of harmonic phasors and power quality in power distribution systems with limited H-PMUs.

Moreover, the prevalent application of H-PMUs in power systems primarily centers on steady-state characteristics, such as monitoring harmonic distortions [30] and assessing power quality [31]. This focus has led to an underutilization of the dynamic potential of harmonic phasor measurements. By harnessing this underexplored dimension, harmonic phasor measurements can capture a more detailed and nuanced picture of power system events, allowing for a deeper understanding and more precise characterization of these oc-

currences. For instance, the enhanced detail provided by harmonic phasor measurements is invaluable in improving the accuracy and granularity of event clustering. Through the use of harmonic phasors, it becomes possible to identify and categorize power system events based on their unique signatures across different harmonic frequencies. This method not only aids in distinguishing between various types of events but also enhances the detection capabilities, leading to more informed decision-making and more effective mitigation strategies in power system operations. The deployment of harmonic phasor measurements can significantly advance the state-of-the-art in event detection and system stability analysis, providing operators with a critical tool for managing the increasingly complex dynamics of modern power systems.

Furthermore, as it was mentioned earlier, the dynamic behavior of modern power systems is increasingly influenced by the proliferation of IBRs, which introduce a level of complexity and unpredictability not previously encountered. In several system-wide incidents, as reported by the North American Electric Reliability Corporation (NERC), the unexpected dynamic response of IBRs to transient disturbances has been identified as a key contributing factor. These incidents have underscored the crucial need for high-resolution monitoring and analysis the rapid and sub-cycle disturbances that characterize the operation of IBRs. In this regards, modeling the sub-cycle dynamics of IBRs is vital for enhancing the situational awareness of utilities and independent system operators (ISOs). It allows for a more precise identification of the types and magnitudes of regional or system-wide disturbances, enabling operators to better anticipate and respond to transient events, thereby mitigating risks and enhancing the overall resilience of the power system. This motivation

drives the need for further research and development in high-resolution monitoring technologies and the implementation of data-driven methods to support the evolving landscape of the power grid.

Therefore, this thesis addresses the challenges of achieving situational awareness in low-observable power distribution systems by leveraging advanced smart grid sensors. It focuses on developing novel data-driven methods for real-time monitoring and dynamic response modeling, utilizing the enhanced capabilities of WMUs and H-PMUs to provide comprehensive insights into the operational status of the power grid. The goal is to improve the reliability and security of power distribution systems in the face of increasing complexity and uncertainty.

1.3 Summary of Contributions

The summary of contributions for each chapter in this thesis are listed as follows: 1) Chapter 2 and 3 presents novel physics-aware harmonic state estimation formulation for low-observable power distribution systems, focusing on extracting unique sparsity patterns from the radial topology. In this regards, we identified physics-based sparsity patterns for harmonic nodal injection current phasors, harmonic line current phasors, and harmonic nodal voltage phasors. Given the scarcity of harmonic measurement sensors in the power distribution feeder, we incorporated these patterns into two different formulations for the HSE problem:

i. In chapter 2, we reformulated the HSE problem as a constrained weighted-Lasso optimization, known as *physics-aware sparse* HSE problem. We considered two scenarios:

- We proposed sparse HSE problem formulation when the *location* of the harmonic source for each harmonic order is known. We formulated a constrained weighted-Lasso optimization problem that incorporates the mathematical implications of the various identified physics-based sparsity patterns.
- We also formulated and solved the sparse HSE problem under a more challenging scenario where the *location* of harmonic source is *not known*. Accordingly, we combine the proposed sparse recovery formulation with a proper exhaustive search in order to enforce the various identified sparsity features despite the lack of prior knowledge about the location of the harmonic source.

ii. In chapter 3, We also reformulated the HSE problem using a *physics-aware MIQP* approach to estimate the number and locations of multiple harmonic sources without prior information:

- We proposed a method to tackle the challenges when there are *multiple* harmonic sources of the *same* harmonic order on the power distribution feeder, while the *number* and *locations* of the harmonic sources are *unknown*. This is a major achievement; specially due to the low-observability of the power distribution system.
- The proposed HSE method integrates the captured physics-aware sparsity characteristics into the formulation of a novel mixed-integer quadratic programming (MIQP) formulation, instead of taking the approach of a typical sparse recovery optimization.

2) In Chapter 4, we adopted a unique multidisciplinary approach to leverage the additional information provided by harmonic phasor signatures for a more in-depth analysis of power system events. This data-driven methodology, viewed through the lens of information theory, is based on real-world H-PMU measurements.

Our analysis identified significant independent information content in the features extracted from event signatures in harmonic phasor measurements. We utilized concepts like normalized mutual information (NMI) and entropy to quantify the additional information captured by harmonic phasors that fundamental phasors cannot. This study explores the following applications of utilizing this additional information content:

- Optimal Harmonic Phasor Order Selection: By applying the normalized mutual information among different set of harmonic phasors' feature data, we show that we can be able to optimally select the orders of harmonic phasors for analyzing power system events, enhancing the ability to identify and interpret these events accurately.
- Event Clustering Enhancement: By integrating harmonic phasor measurements with fundamental phasor data, we demonstrate a significant improvement in event clustering tasks. This enhancement is quantitatively shown through the use of silhouette values, indicating the better-defined clustering of events when incorporating the harmonic feature space.

3) In chapter 5, Utilizing real-world data from Waveform Measurement Units, we proposed novel data-driven methods to model the dynamic response of inverter-based resources to high-frequency disturbances in power systems. In this regards, We treated the IBR as a black-box with an input of voltage waveform and an output of current waveform. After ex-

tracting differential voltage waveforms and differential current waveforms from raw data, we developed multiple methods, including data-driven model library construction and proper model selection.

i. We proposed methods in the frequency domain based on modal analysis:

   - Applying modal analysis techniques, such as the Prony method, to express differential voltage and current waveforms as sums of dynamic modes characterized by angular frequency and damping factors. We used these modes to build a library of equivalent admittance models.
   - Selecting the appropriate model from this library to estimate the IBR's response to disturbances by identifying the mode closest to the test input signal's dynamic mode.

ii. We proposed methods in the time domain based on regression analysis of time-series data:

   - Using Finite Impulse Response (FIR) models to estimate the IBR's response as weighted sums of recent samples from the input signal.
   - Employing Auto-Regressive eXogenous (ARX) models to estimate the IBR's response using recent samples from both the input signal and its own output signal.
   - Constructing a model library from training data and selecting the appropriate model by directly comparing the time series of the test input signal with those of the training input signals.

1.4 Definitions

The following technical terms are used throughout this thesis:

Harmonics: Harmonics refer to the sinusoidal components of a periodic waveform that are integer multiples of the fundamental frequency. These components distort the waveform and can cause various power quality issues in power systems.

Harmonic Phasor Measurement Unit (H-PMU): A Harmonic Phasor Measurement Unit is an advanced measurement device that extends the capabilities of conventional Phasor Measurement Units (PMUs) by also measuring the harmonic phasors. This allows for detailed monitoring and analysis of harmonics in the power system.

Harmonic State Estimation (HSE): Harmonic State Estimation is a technique used to estimate the magnitudes and phases of harmonic components of the state variables in a power system. This helps in identifying the sources and propagation of harmonics, thereby enhancing the situational awareness of power distribution systems.

Inverter-Based Resources (IBRs): Inverter-Based Resources are power generation sources that use inverters to convert direct current to alternating current. Examples include solar photovoltaic systems, wind turbines, and battery storage systems. IBRs are critical for integrating renewable energy into the power grid.

Cycle: In a power system operating at 60 Hz, one cycle is completed in 1/60 seconds, or approximately 16.67 milliseconds.

Event: An event (or a disturbance) in the context of power systems refers to any significant occurrence that affects the normal operation of the system. Events can include faults, switching operations, load changes, and other disturbances.

Transient Event: A transient event is a temporary disturbance in the power system that lasts for a short duration, ranging from less than a cycle (sub-cycle), to up to four cycles (multi-cycle). These events can include sudden voltage changes, current surges, or other brief anomalies that can impact system stability and equipment.

Waveform Measurement Unit (WMU): A smart grid sensor used to capture high-resolution time-domain waveforms of electrical signals. WMUs provide detailed data on voltage and current waveforms, which are essential for analyzing dynamic behaviors and disturbances in the power system.

Chapter 2

Physics-Aware Sparse Harmonic State Estimation in Power Distribution Systems

2.1 Introduction

2.1.1 Background and Motivation

Harmonic pollution has often been the cause of failures which severely affect reliable operation of power systems [32]. As discussed in Chapter 1, it is highly important in modern power systems to develop situational awareness regarding harmonic distortions. Harmonic state estimation is crucial in achieving situational awareness about harmonics.

Although the cost of power quality sensors is dropping, it is still impractical to maintain full-observability about harmonic distortions by placing power quality sensors at

every bus. That raises the question on how can we achieve situational awareness about harmonics in power distribution systems, while using only a few harmonic phasor measurement sensors. In this chapter, we seek to address this open problem.

2.1.2 Related Works and Contributions

Although extensive research has been conducted on the study of Harmonic State Estimation at the transmission level [33, 34, 35, 36, 37, 38], developing HSE methods at power distribution networks requires addressing its own unique issues. These challenges stem from the fundamental differences between power transmission and distribution systems, which prevent the direct application of transmission system state estimation methods to distribution systems. For instance, power distribution systems are often highly unbalanced [25], while state estimation methods, including HSE, are typically designed for the balanced operation of power transmission networks. This imbalance increases the complexity of the power flow equations, requiring the use of a three-phase model instead of a single-phase equivalent. Furthermore, power distribution lines generally have a higher resistance to reactance ratio, making the DC power flow equations used in transmission state estimation methods inaccurate for distribution systems [26]. As a result, the power flow equations for state estimation in distribution systems must be formulated using AC power. Lastly, the high penetration of renewable energy resources introduces significant uncertainty into HSE at the distribution level. This uncertainty affects aspects such as network topology and line parameters, further complicating the HSE process compared to that in transmission systems [28, 29].

For a radial or weakly-meshed power distribution system, numerous harmonic measurement devices are needed to make the system fully-observable. Therefore, due to the lack of extensive monitoring at the distribution level, a necessary requirement in any HSE method at distribution level is to address the issue of low-observability [24, 39, 40, 41].

A common approach to make up for the lack of measurements in the HSE problem is to use pseudo-measurements such as historical data. But in this case, the error and uncertainty in the historical data can severely affect the accuracy of HSE.

Another approach is not to use pseudo-measurements, but rather to directly deal with the low-observability conditions by using mathematical techniques to solve the HSE problem as an undetermined system of equations. In [39], the HSE problem is solved by using singular value decomposition, where the HSE problem is formulated as a least square optimization and solved by obtaining the pseudo-inverse of the low-rank measurement matrix. In [24], a method is proposed to solve the HSE problem based on sparse Bayesian learning which involves regression analysis for power flow calculation and recurrent neural network models for demand prediction in power distribution systems. In [37], the HSE problem is formulated as a constrained sparsity maximization problem which is solved by using linear programming.

However, to the best of our knowledge, the prior studies in the literature have not taken the unique physics-based features of the power distribution system into account, such as its radial topology, as the main tool in achieving sparse recovery. As a result, they still require a considerably large number of sensors to be deployed. Thus, there is still a need to explore some of the most important sparsity patterns in the state variables of

the power distribution system, while the physics-based relations and constraints among the state variables are being considered.

In this study we propose a novel physics-aware sparse HSE method in power distribution systems with very few power quality sensors. The proposed method is built upon extracting some unique sparsity patterns in power distribution systems based on their radial topology and other physical characteristics.

2.2 Problem Formulation

Let $\mathcal{G} := (\mathcal{N}, \mathcal{L})$ denote the graph representation of a power distribution feeder, where $\mathcal{N}$ is the set of nodes and $\mathcal{L}$ is the set of distribution lines. For a harmonic order h, let $\mathbf{I}_N(h)$ denote the vector which contains the nodal harmonic injection current for all the nodes in set $\mathcal{N}$. Also, let $\mathbf{I}_L(h)$ denote the vector of harmonic line currents for all the line segments in set $\mathcal{L}$ for harmonic order h. Let $\mathbf{V}(h)$ denote the vector of nodal harmonic voltage phasors for all the nodes in set $\mathcal{N}$ for harmonic order h. In our problem formulation, the vector of state variables for each harmonic order h is denoted by

$$\mathbf{X}(h) = [\, \mathbf{I}_N(h) \;\; \mathbf{I}_L(h) \;\; \mathbf{V}(h) \,]^\top. \tag{2.1}$$

Suppose there are only a few harmonic phasor measurement units available across the distribution feeder to measure the harmonic nodal voltage phasors $\mathbf{V}^m(h)$ and the harmonic line current phasors $\mathbf{I}_L^m(h)$ at the locations of H-PMU installations. Let $\mathbf{Z}(h)$ denote the measurement vector:

$$\mathbf{Z}(h) = [\, \mathbf{V}^m(h) \;\; \mathbf{I}_L^m(h) \,]^\top. \tag{2.2}$$

The goal in HSE is to estimate the state variables $\mathbf{X}(h)$ based on the available measurements $\mathbf{Z}(h)$.

2.2.1 Basic Equations

Since all the harmonic measurements are in phasor domain, the following relationship holds between the harmonic phasor measurements and the harmonic state variables:

$$\mathbf{Z}(h) = \mathbf{H}(h)\,\mathbf{X}(h), \tag{2.3}$$

where $\mathbf{H}(h)$ is the measurement matrix at harmonic order h. Next, we explain the construction of matrix $\mathbf{H}(h)$.

The first type of equations in matrix $\mathbf{H}(h)$ are associated with harmonic voltage phasor measurements. The following relationship holds between the nodal harmonic injection current phasors and the harmonic voltage phasor measurements:

$$\mathbf{V}^m(h) = \mathbf{Y}^{-1}(h)\,\mathbf{I}_N(h), \tag{2.4}$$

where $\mathbf{Y}(h)$ is the admittance matrix for harmonic order h. In addition to (4), the harmonic voltage phasor measurements can be mapped also to their associated entries in the vector of harmonic voltage phasors through an identity mapping:

$$\mathbf{V}^m(h) = \mathbf{U}\,\mathbf{V}(h), \tag{2.5}$$

where $\mathbf{U}$ is a diagonal matrix, where a diagonal entry is 1 if its corresponding state variable is a harmonic voltage phasor that is directly measured; otherwise it is 0.

The second type of equations in matrix $\mathbf{H}(h)$ are associated with the harmonic line current measurements. The harmonic line current measurements are mapped to the vector of nodal harmonic voltage phasors as follows:

$$\mathbf{I}_L^m(h) = \mathbf{Y}_{\text{prim}}(h)\ \mathbf{V}(h), \tag{2.6}$$

where $\mathbf{Y}_{\text{prim}}(h)$ is the primitive admittance matrix [42], which includes the line admittances only for the line segments whose harmonic current phasors are measured. Harmonic line current phasor measurements can also be related to the vector of the harmonic line current phasors through an identity mapping:

$$\mathbf{I}_L^m(h) = \mathbf{U}\,\mathbf{I}_L(h), \tag{2.7}$$

where $\mathbf{U}$ is a diagonal matrix, where a diagonal entry is 1 if the corresponding state variable is a harmonic current phasor that is directly measured; otherwise it is 0.

2.2.2 Additional Equations

The equations in (2.4)-(2.7) capture all the basic relationships between the entries of vector $\mathbf{Z}(h)$ and those of vector $\mathbf{X}(h)$. We can use the equations in (2.4)-(2.7) to construct matrix $\mathbf{H}$. However, due to the limited measurements, which is due to the limited number of H-PMU installations in practice, matrix $\mathbf{H}(h)$ is a *low-rank* matrix. Thus, the system of equations in (2.3) has an infinite number of solutions; which is not desirable.

The main remedy to the above issue is the use of sparsity analysis as we will see in Section 2.3. However, it is useful to also add more equations to the basic set of equations in (2.4)-(2.7). In particular, we need to create more couplings among the state variables, even

though such additional couplings does *not* make matrix $\mathbf{H}(h)$ full-rank. To do so, for the line segments that do not come with a direct harmonic phasor measurement, we propose to write an equation similar to (2.6), as follows:

$$\mathbf{0} = \mathbf{Y}_{\text{prim}}(h)\, \mathbf{V}(h) - \mathbf{I}_L(h). \tag{2.8}$$

Unlike in (2.6), the equations in (2.8) are *not* based on measurements; but they do serve the purpose of further coupling the state variables. Here they act as auxiliary equations.

We can treat the zeros on the left hand side in (2.8) as virtual measurements to revise the vector of measurements in (2.2) as:

$$\mathbf{Z}(h) = [\, \mathbf{V}^m(h) \;\; \mathbf{I}_L^m(h) \;\; \mathbf{0} \,]^\top. \tag{2.9}$$

2.2.3 Original HSE Formulation

If the power distribution feeder is fully observable at harmonic order h, then we can formulate the HSE problem as:

$$\min_{\mathbf{X}(h)} \;\; ||\mathbf{Z}(h) - \mathbf{H}(h)\, \mathbf{X}(h)||_2^2. \tag{2.10}$$

However, if the network is *not* fully observable, i.e., if we only have a few H-PMUs, then solving the above problem does not lead to a meaningful solution. Therefore, for the rest of this paper, we seek to address this open problem by making use of concepts from sparse recovery in signal processing.

2.3 Physics-Based Sparsity Features

From the theory of sparse recovery in signal processing, when it comes to an undetermined system of linear equations, such as the one in (2.3), if the unknown vector is *sparse*, then we might be able to obtain the unique solution of the undetermined system of linear equations despite the low observability conditions [43]. To do this, we need to first identify and extract the inherent sparsity patterns in the physical system.

Consider the IEEE 33-bus distribution test network in Fig. 2.1. Suppose there is a harmonic current source at bus 13. As it is previously shown in [11, 44, 45], the harmonic current in this power distribution feeder almost entirely flows through the substation and *not* through the loads. The reason is that the impedance in the Thevenin equivalent of the substation that is seen by the distribution feeder is much less than the impedance of the loads across the distribution feeder. Therefore, almost the entire harmonic current that is injected by the harmonic source at bus 13 passes through the line segments that are marked with red color, all the way up to the substation.

The above physical observation can be used as the foundation to introduce sparsity to harmonic state estimation. Based on the notations that we defined in Section 2.2, the sparsity is primarily in the vector of nodal harmonic current injection, i.e. $\mathbf{I}_N(h)$. Since only one harmonic source of each harmonic order is assumed to be in the network, only one entry in $\mathbf{I}_N(h)$ is non-zero, which is associated with the node of the harmonic source. The rest of the entries in $\mathbf{I}_N(h)$ are zero.

There is also a major sparsity in the vector of harmonic line current phasors, i.e., $\mathbf{I}_L(h)$. Recall from Fig. 2.1 that only the line segments on the red path between the

harmonic source and the substation carry harmonic current. Therefore, only the entries in $\mathbf{I}_L(h)$ that are associated with the line segments on the red path are non-zero. All the other entries in $\mathbf{I}_L(h)$ that are associated with the line segments that are outside the red path are almost zero. Moreover, all the line segments that are on the red path have almost *equal* harmonic current; because the harmonic current almost entirely flows to the substation.

The above analysis also has implications for the harmonic voltage phasors. Since there is harmonic line current on the red path in Fig. 2.1, the nodal voltage for all the buses on this red path include *some* level of harmonic distortion associated with the same harmonic source. However, the story is a bit different for the nodes that are *outside* the red path.

To see this, let us first *group* the nodes that are *outside* the red path such that all the nodes that are laid on the same lateral are put in the same group; see [46] for a similar grouping idea. For example, buses 26, 27, 28, 29, 30, 31, 32, and 33 form one group in Fig. 2.1. Bus 6 is the *boundary node* for this group. For any such group, if there is no (almost no) harmonic component in the voltage at the boundary node, then there is zero (almost zero) harmonic component in the voltage of *all* the nodes in the group; otherwise, there is non-zero harmonic component in the voltage of *all* the nodes in the group. If all of the harmonic voltage phasors are non-zero in a group, they are *equal* to the harmonic voltage phasor at the boundary node.

For example, again consider buses 26 to 33 in Fig. 2.1 which are outside the red path and on the same lateral. They form one group. For all the nodes in this group, all would have *equal* nodal harmonic voltage phasors. If there is zero (or almost zero)

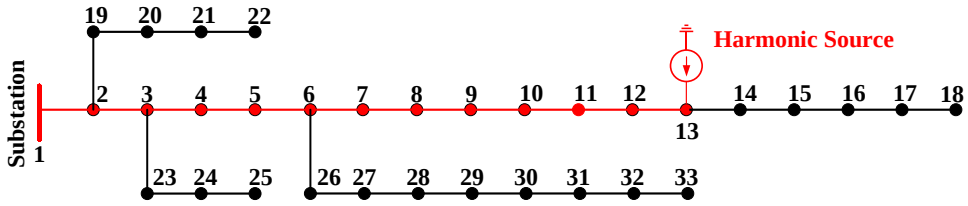

Figure 2.1: An example distribution feeder with one harmonic source. In practice, the harmonic current almost entirely flows through the substation.

harmonic component in the voltage at the boundary node, i.e., bus 6, then there would be zero (or almost zero) harmonic component in the voltages at buses 26 to 33. If there *is* a considerable harmonic component in the voltage at bus 6, then there would be an equal harmonic component in the voltages at buses 26 to 33. This is because there is *no* harmonic current flowing on any of the lines between the nodes in the above group of nodes. Thus, in addition to the sparsity in harmonic current phasors $\mathbf{I}_N(h)$ and $\mathbf{I}_L(h)$, there is also a group sparsity in the nodal harmonic voltage phasors $\mathbf{V}(h)$. We can enforce all these various sparsity patterns by constructing the following additional equality constraint in our problem formulation:

$$\mathbf{A}\,\mathbf{X}(h) = \mathbf{0}. \tag{2.11}$$

The rows are corresponding to two types of equality constraints: 1) the harmonic line current phasors are equal for all the line segments on the path between the substation and the node where the harmonic source is located; and 2) the harmonic voltage phasors are equal at the nodes within each group, including the boundary node of the group.

For instance, in the example that we mentioned earlier, to set the harmonic voltage phasor at bus 26 to be equal to the harmonic voltage phasor at bus 6, we need a row in

matrix $\mathbf{A}$ to include 1 as the coefficient to the harmonic voltage phasor at bus 6; and -1 as the coefficient to the harmonic voltage phasor at bus 26. Notice that, one single constraint in matrix form can capture all such equalities across all the groups. The same holds for the equality of harmonic line currents.

Remark 1: The assumption that the network topology is radial is necessary for the proposed method. For the case of a *weakly* meshed network, we may still apply our method to the radial sub-segments of the network. We may also take a meshed sub-segment of the network as a *super-node*, thus reducing the weakly meshed network topology to radial topology with a few super-nodes for applying our proposed method. However, for a meshed network topology, such as in some micro-grids, our method may no longer be applicable.

Remark 2: The sparsity patterns that we discussed in this section are based on the assumption that there is only one harmonic source of the same harmonic order on the distribution feeder. Of course, we can have multiple harmonic sources of *different* harmonic orders. If there are multiple harmonic sources of the same order, then our method may still work; however, as the number of harmonic sources increases, the sparsity in state variables diminishes, which might degrade the performance of the method. Addressing this issue is beyond the scope of this paper and can be studied in a future work.

2.4 HSE with Sparse Recovery

Methods from compressed sensing and sparse recovery can be used to obtain the solution of the undetermined system of equations in (2.3). In this regard, we can formulate the HSE problem as a Lasso optimization problem [43]:

$$\min_{\mathbf{X}(h)} \quad \frac{1}{2}||\mathbf{Z}(h) - \mathbf{H}(h)\ \mathbf{X}(h)||_2^2 + \lambda||\mathbf{X}(h)||_1. \tag{2.12}$$

The first term in the objective function is the least square error in state estimation. The use of ℓ_1-norm in the second term is a common approach in sparse recovery to minimize the number of non-zero state variables, where λ is a penalty factor.

Although the Lasso optimization in (2.12) treats $\mathbf{X}(h)$ as a sparse vector, it does not distinguish between its entries. Whilst, in our discussion in Section 2.3, we extracted valuable information about the sparsity pattern of the specific entries in vector $\mathbf{X}(h)$ based on the physics of the system. Hence, we need to reflect that information in the the problem formulation. This raises the question on how this would be done if:

1) The location of harmonic source is *known*,

2) The location of harmonic source is *unknown*.

2.4.1 Known Location of Harmonic Source

In this scenario, we assume that the location of the harmonic source is known. We know *which entry* in the nodal harmonic current injection vector $\mathbf{I}_N(h)$ is non-zero; however, its value is still *not* known and it must be estimated by the HSE. Similarly, we know which entries in vector $\mathbf{I}_L(h)$ are non-zero; but we do *not* know their values. We also know which entries in vectors $\mathbf{I}_L(h)$ and $\mathbf{V}(h)$ are in the same group.

To incorporate the above information to the sparse recovery process, we reformulate the Lasso optimization in (2.12), and present it as a *constrained weighted-Lasso* optimization [47]:

$$\begin{aligned} \min_{\mathbf{X}(h)} \quad & \frac{1}{2}\mathbf{Z}(h) - \mathbf{H}(h)\ \mathbf{X}(h)_2^2 + \lambda \mathbf{W}\mathbf{X}(h) \\ \text{s.t.} \quad & \mathbf{A}\ \mathbf{X}(h) = \mathbf{0}. \end{aligned} \tag{2.13}$$

where $\mathbf{W}$ is a vector which contains the *weight* for each entry in vector $\mathbf{X}(h)$ to enforce the extracted sparsity patterns. If an entry in $\mathbf{X}(h)$ is known to be zero, then a large weight is used in $\mathbf{W}$ to create a large penalty to push the value toward zero. In contrast, for the entries in $\mathbf{X}(h)$ that are known to be non-zero, we only use a small weight in $\mathbf{W}$ to create a small penalty for that entry such that it does not grow.

Problem (2.13) is convex. We can use any convex optimization solver, such as CVX toolbox [48], to solve it.

2.4.2 Unknown Location of Harmonic Source

As a more challenging scenario, next, we assume that the location of the harmonic source is *not* known. Hence, we do *not* know which exact entries are zero in advance.

Nevertheless, all the sparsity patterns that we extracted in Section 2.3 are still valid. Therefore, we can still solve this more challenging case by combining the method in Section 2.4.1 with an exhaustive search. The idea is as follows:

If we *assume* a tentative location for the harmonic source, we can use the exact formulation as in (2.13) to solve the HSE problem by using the sparsity patterns based on such tentative assumption. Suppose we *assume* that bus k is the location of the harmonic source; and accordingly, we obtain $\mathcal{R}_k$ as the corresponding *residue* when we solve the optimization problem in (2.13). In other words, $\mathcal{R}_k(h)$ is the optimal objective value of the optimization in (2.13) based on the *assumption* that the harmonic source is at bus k.

Therefore, by taking each of the buses in the network as the location of the harmonic source and solving the optimization problem in (2.13) accordingly, we can identify the *unknown* location of the harmonic source at harmonic order h as:

$$k^\star = \arg\min_k \mathcal{R}_k(h). \tag{2.14}$$

The above problem can be solved by using an exhaustive search. This requires to solve N optimization problems of the form in (2.13), where N is the number of buses in the network. Once we obtain $\mathcal{R}_k(h)$ for each $k = 1, \ldots, N$, we can obtain $k^\star$ by simply taking the minimum of the N obtained residues.

Once $k^\star$ is obtained, the analysis in this section reduces to the same analysis in the first scenario in Section 2.4.1.

2.5 Case Studies

We apply the proposed physics-aware sparse HSE method to the IEEE 33-bus distribution test system [49]. All the case studies are simulated in the Open Distribution System Simulator (OpenDSS) [50]. Six H-PMUs are assumed to be installed at the substation and at nodes 6, 18, 22, 25, and 33.

2.5.1 Performance Comparison

We compare the performance of the proposed physics-aware sparse HSE method with two other methods: 1) the sparse HSE but without utilizing the physics-based knowl-

Table 2.1: Performance comparison of different HSE methods for harmonic order $h = 3$

Method	MSE $\mathbf{V}$	STD $\mathbf{V}$	MSE $\mathbf{I}_L$	STD $\mathbf{I}_L$
Physics-Aware Sparse HSE	0.0174	0.094	0.00275	0.0274
Method in [37]	223.8	7.56	13.34	2.53
Method in [39]	221.1	7.368	9.79	2.512

edge, i.e., the method in [37]; and 2) the method in [39] which works based on singular value decomposition. We use the Mean Square Error (MSE) as the metric to compare the performance of different HSE methods:

$$\text{MSE} = \frac{1}{N}||\mathbf{X}_{act}(h) - \mathbf{X}_{est}(h)||_2^2, \tag{2.15}$$

where N is the number of unknown harmonic state variables.

Table I shows the results based on the mean and the variance of the MSE index; which are calculated separately for the unknown harmonic nodal voltages, denoted by MSE $\mathbf{V}$ and STD $\mathbf{V}$, and for the unknown harmonic line currents, denoted by MSE $\mathbf{I}_L$ and STD $\mathbf{I}_L$. The harmonic source is assumed to be of harmonic order $h = 3$. The magnitude of the injected harmonic current is assumed to vary randomly between 10% to 50% of the load at the location of the harmonic source. We assume that the location of the harmonic source is known.

As we can see, the proposed method has a drastically lower average MSE and standard deviation in comparison with the method in [39] and the sparse HSE without physics-awareness.

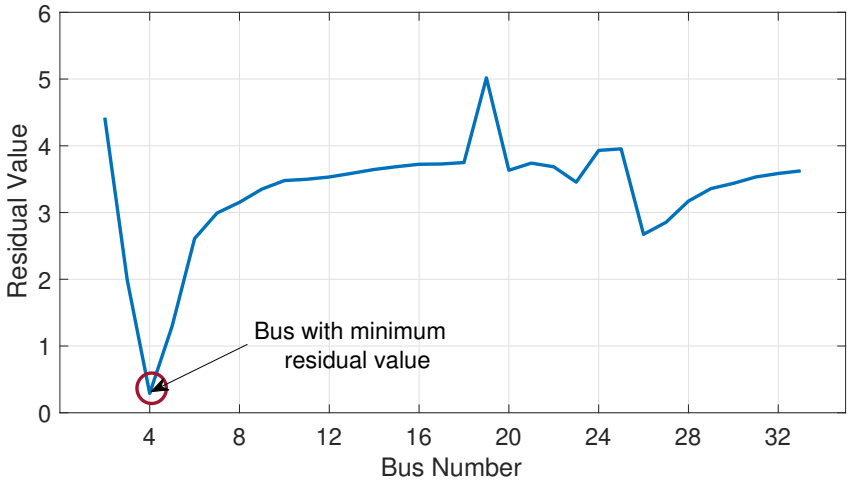

Figure 2.2: Residue $\mathcal{R}_k(h)$ versus the candidate location of the harmonic source. The location of the harmonic source is *not* known in advance.

2.5.2 Unknown Location of Harmonic Source

Next, we assume that the location of the harmonic source is not known. Accordingly, we use the proposed method in Section 2.4.2. The results from the exhaustive search are shown in Fig. 2.2. Here, we plotted the Residue $\mathcal{R}_k(h)$ versus the candidate location of the harmonic source at buses $k = 2, \ldots, 33$. We can see that the minimum residue is obtained at $k^\star = 4$. This is indeed the correct location of the event bus; which confirms the effectiveness of the proposed method even when the location of the harmonic source is not known.

2.5.3 Sensitivity Analysis: Harmonic Order

In practice, the magnitude of harmonic source may vary depending on the harmonic order. Thus, to have a fair assessment, we compare the normalized MSE for voltages for different harmonic orders. The results are shown in Fig. 2.3. We can see that the

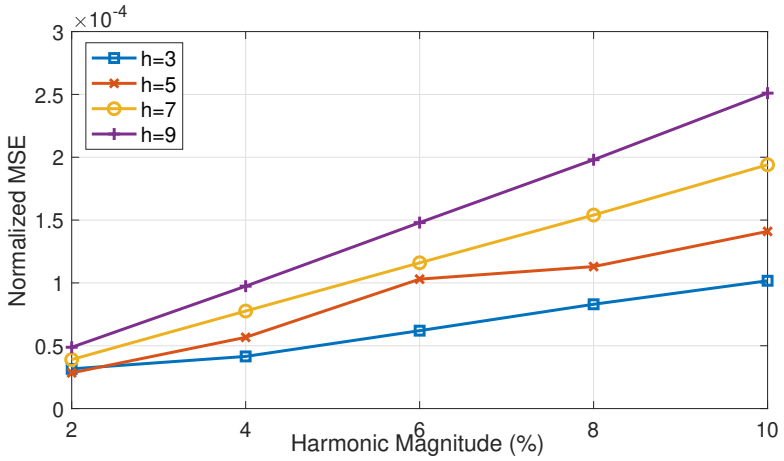

Figure 2.3: Comparing the results at different harmonic orders.

normalized MSE increases as we increase the harmonic order as well as the magnitude of harmonic source.

2.5.4 Sensitivity Analysis: Location of the Harmonic Source

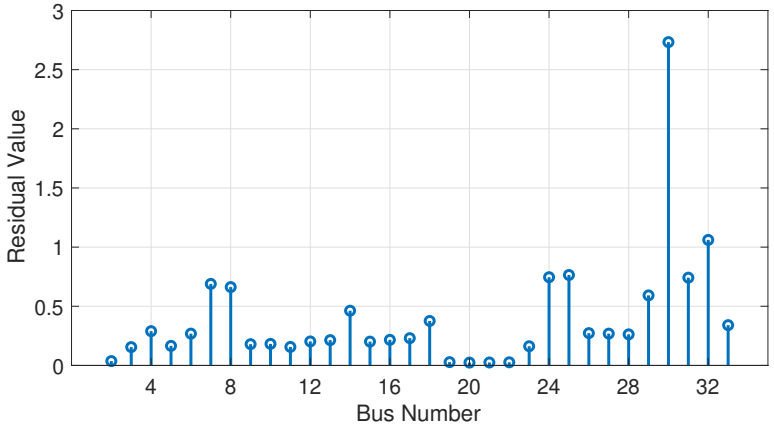

Figure 2.4: HSE residue versus the location of the harmonic source, where $h = 3$.

Fig. 2.4 shows the HSE residue, i.e., the optimal objective value of the HSE optimization problem, for all the possible scenarios for the location of the harmonic source.

We can see that, as the distance of the harmonic source from the substation grows, the performance of the HSE method gradually degrades. This is due to the fact that a longer distance for the harmonic source from the substation means a *less sparse* scenario. Also, when distance increases, the estimation error increases as well; because the observability over the nodes that are far from the sensors is lowered. As a result, as we move to bus 33, the HSE estimation error increases in general.

Chapter 3

A Physics-Aware MIQP Approach to Harmonic State Estimation in Low-Observable Power Distribution Systems Using Harmonic Phasor Measurement Units

3.1 Introduction

3.1.1 Background and Motivations

Modern power systems have increasingly become reliant on power electronic devices, nonlinear loads, and inverter-based energy resources. These technologies, while beneficial, have significantly contributed to the rise in harmonic distortions within power distribution systems. Harmonic pollution can jeopardize the reliability and safety of the grid, leading to conductor overheating and interference with protection systems [2]. Consequently, utilities are mandated to monitor and manage harmonic levels to ensure system integrity [51].

As noted in Section 2.1.1, Harmonic State Estimation is critical in developing a comprehensive real-time monitoring system, enabling operators to identify harmonic sources and track their propagation across the distribution network. However, the widespread installation of Harmonic Phasor Measurement Units is hindered by high costs and impracticalities. This raises the question of how we can achieve situational awareness of harmonic phasors and power quality in power distribution systems while using only a few H-PMUs.

In Chapter 2, we proposed a solution to maximize grid harmonic visibility with limited H-PMU deployment However, there are limitations to this approach. 1) The method requires prior knowledge of the harmonic source's location. In the absence of such information, an exhaustive search across the network becomes necessary, which can be computationally expensive, particularly for large-scale power networks. 2) the method is most effective in scenarios involving a single harmonic source. Performance decreases significantly as the number of harmonic sources increases due to reduced sparsity of the state variables.

In this chapter, we propose a novel formulation for the HSE problem that seeks to overcome these limitations. Our enhanced approach is designed to improve the robustness and efficiency of HSE, even in complex power systems with multiple harmonic sources even for each harmonic order. By refining the model and algorithm, we aim to provide a more practical and scalable solution for achieving effective situational awareness in modern power distribution systems.

3.1.2 Related Work

While there is a rich literature on the study of HSE at the transmission level [33, 34, 35, 36, 37, 38], the literature on the study of the HSE at the distribution level is still limited [52, 53, 54, 24, 39, 40]. This is because, HSE is a relatively new problem at power distribution systems in practice. It has been emerging as a viable effort only recently due to the recent advancements in instrumentation and sensor deployments at power distribution systems.

However, there are major differences between conducting HSE at the transmission level and conducting it at the distribution level. There are at least two reasons for these differences. The first issue is the lack of measurement redundancy at distribution level; even lack of sufficient measurements to achieve basic observability. Importantly, most of the existing HSE methods are meant to be used at transmission level with sufficient harmonic phasor measurements such that the network is *fully-observable* [27]. The second issue is the nature of all radial topologies in power distribution networks. Inherently, there is *less coupling* among the harmonic voltage phasors across different buses in a radial network topology; because each bus has at most only two immediate neighboring buses. This is very

different from the tight coupling among the harmonic voltage phasors in a meshed network topology, which is common in power transmission systems. Therefore, one cannot simply reuse the HSE methods that are developed for the transmission level at the distribution level. For a power distribution system that has a radial topology, numerous harmonic measurement devices (and their associated communication infrastructures) are needed in order to make the system fully-observable; but this is cost prohibitive.

Therefore, the ability to work under the *low-observability* conditions is a necessary feature for an effective HSE method that is meant to be used in power distribution networks.

Accordingly, we can divide the existing literature on HSE at power distribution systems into two groups. First, the HSE methods that do *not* explicitly address low-observability, e.g., in [53, 54, 55]. Second, the HSE methods that *do* explicitly mention the need to address low-observability [24, 52, 39, 40].

The methods in the first group usually fail to provide accurate results when the network is *not* observable. This is because they are *not* designed to work under such circumstances.

As for the methods in the second group, that do recognize the need to address low-observability in the HSE problem at distribution level, a common approach is to use pseudo-measurements (such as historical data) to make the network fully-observable, e.g., see [56, 53]. However, uncertainty and error in historical data have huge impact on the accuracy of the HSE methods that need to rely on pseudo-measurements.

Another approach to tackle low-observability in the HSE problem is to use mathematical techniques to deal with the rank deficiency of equations in the HSE problem. In

[52, 39], HSE methods are proposed based on singular value decomposition to formulate the HSE problem at distribution level as a least square optimization and to solve it by obtaining the pseudo-inverse of the low-rank measurement matrix. In [24], an HSE method is proposed based on sparse Bayesian learning which involves using regression for power flow analysis and recurrent neural network models for demand prediction.

In [37], the HSE problem is formulated as a constrained sparsity maximization which is solved by linear programming. Although this work was tested on the 14-bus power transmission system, since the methodology does not depend on the inherent properties of the transmission level, it has the basic capabilities to be applied to power distribution systems as well. Compressed sensing is used also in [57], where the focus is on the case with only one harmonic source in the network.

Although sparse recovery is considered effective in finding the sparse solution for an undetermined system of equations, the mathematical conditions that may guarantee its performance are usually very specific and do not hold in the HSE problem, specially if there is *more than one* harmonic source of the same harmonic order in the system [57].

There are also methods that are *not* meant to solve the HSE problem; but they seek to estimate and identify the location of the harmonic source(s) at the distribution level [58, 59, 27, 41]. These methods are very different from HSE; because they do *not* estimate the harmonic state variables across the power distribution network. In [58], a Bayesian approach is proposed to locate the harmonic source. In this method, the information to indicate the possible presence of the harmonic source as well as a metric about the reliability of such metric are discussed. In [59], a method is proposed based on particle

swarm optimization to locate and estimate the parameters of the harmonic source with the highest contribution. In [27], a method based on exhaustive search is developed to locate and estimate multiple sources of harmonics in a low-observable power distribution system. Importantly, the methods in [58, 59, 27, 41] are *not* designed to solve the HSE problem.

Another subject that is widely discussed in the literature is the task of sensor placement in power systems, including the placement of harmonic sensors. Different methods have been used, such as integer programming [60], quadratic programming [61], genetic algorithm [62] and neural networks [63]. However, sensor placement is beyond the scope of this paper.

Last but not least, it is worth emphasizing that, when it comes to the HSE problem, the issue with low-observability is with respect to the *harmonics* in the system. It is *not* with respect to the *fundamental* component. It is possible that a power distribution system *is* observable at the fundamental frequency, but it is *not* observable at the harmonics. Note that, observability at the fundamental frequency can be achieved or reinforced by using different types of sensors, including PMUs and smart meters, which are widely deployed by many utilities. Therefore, there can be several sensors available for an ordinary state estimation at the fundamental frequency. The literature on addressing low-observability in ordinary (i.e., not harmonic) distribution system state estimation is separate, such as in [64, 46, 65, 66]. However, in practice, we have a few harmonic sensors available for harmonic state estimation. Consequently, it might be possible for a power system to be observable at the fundamental frequency, but not at certain harmonics.

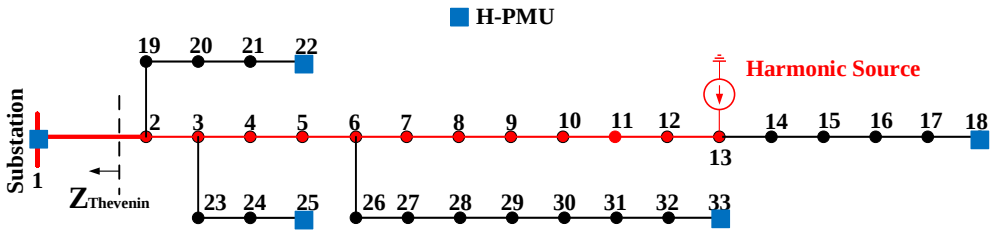

Figure 3.1: An example distribution feeder with one harmonic source. In practice, the harmonic current almost entirely flows through the substation.

3.2 System Model

Let $\mathcal{G} := (\mathcal{N}, \mathcal{L})$ denote the graph representation of a radial power distribution feeder, where $\mathcal{N}$ is the set of all buses and $\mathcal{L}$ is the set of all line segments. An example is shown in Fig. 3.1, where the network topology is based on the IEEE 33-bus test system. For each harmonic order h in the system, we assume that $\mathbf{I}_N(h)$ denotes the vector of the harmonic nodal current injection phasors at all the buses in set $\mathcal{N}$. Similarly, let $\mathbf{I}_L(h)$ denote the vector of the harmonic line current phasors at all the line segments in set $\mathcal{L}$; and let $\mathbf{V}(h)$ denote the vector of the harmonic nodal voltage phasors at all the buses in set $\mathcal{N}$.

3.2.1 Basic HSE Problem Formulation

At each harmonic order h, we define the vector of the harmonic state variables in the power system as follows:

$$\mathbf{X}(h) = [(\mathbf{I}_N(h))^\top (\mathbf{I}_L(h))^\top (\mathbf{V}(h))^\top]^\top. \tag{3.1}$$

Our goal is to estimate the above vector of state variables by using harmonic synchrophasor measurements from H-PMUs. Each H-PMU measures the harmonic nodal voltage phasors and the harmonic line current phasors at its location.

Let $\mathbf{Z}(h)$ denote the vector of all available harmonic synchrophasor measurements that are collected from the H-PMUs:

$$\mathbf{Z}(h) = [(\mathbf{V}^m(h))^\top (\mathbf{I}_L^m(h))^\top]^\top, \tag{3.2}$$

where superscript m indicates the measurements to distinguish them from the state variables. Also, let us define $\mathbf{H}(h)$ as the harmonic measurement matrix, which captures all the mappings between the harmonic synchrophasor measurements in $\mathbf{Z}(h)$ and the harmonic state variables in $\mathbf{X}(h)$ as:

$$\mathbf{Z}(h) = \mathbf{H}(h)\, \mathbf{X}(h) + \mathbf{e}(h), \tag{3.3}$$

where $\mathbf{e}(h)$ is the corresponding vector for measurement noise. The construction of matrix $\mathbf{H}(h)$ is discussed in Appendix A.

The HSE problem is then formulated as follows:

$$\underset{\mathbf{X}(h)}{\textbf{minimize}} \ \left\|\mathbf{Z}(h) - \mathbf{H}(h)\mathbf{X}(h)\right\|_2^2. \tag{3.4}$$

If matrix $\mathbf{H}(h)$ is full-ranked, then the network is fully-observable at harmonic order h and the least-square problem in (3.4) has a unique solution. This happens only if we install a large number of H-PMUs across the distribution circuit.

3.2.2 Augmented HSE Problem Formulation

A power system is said to be *fully-observable* in the domain of harmonics, if the harmonic state variables at all buses and/or all line segments can be uniquely obtained from the available harmonic phasor measurements. An analytical interpretation of full-

observability is that the measurement matrix $\mathbf{H}(h)$ must be full-rank. To achieve full-observability in a radial power distribution feeder, the grid operator must install H-PMUs at least at half of the buses. However, this is *not* a realistic option, because of the high cost of H-PMUs, including the cost of sensors, the cost of sensor installation, and the cost of setting up a communication infrastructure for data collection. As a result, power distribution systems are often inherently subject to low-observability, specially when it comes to solving the HSE problem. For instance, for the case of the network in Fig. 3.1, we may face a scenario where only five H-PMUs are available; one at the substation; one at the end of the main; and three at the end of each of the three laterals.

Therefore, in practice, the network is *not* fully-observable; and it is a challenge to solve the HSE problem in (3.4).

To properly address this challenge, we focus on an *augmented* version of the HSE problem as follows:

$$\underset{\mathbf{X}(h)}{\textbf{minimize}} \left\| \begin{bmatrix} \mathbf{Z}(h) \\ \\ \mathbf{0} \end{bmatrix} - \begin{bmatrix} \mathbf{H}(h) \\ \\ \mathbf{G}(h) \end{bmatrix} \mathbf{X}(h) \right\|_2^2, \tag{3.5}$$

where $\mathbf{G}(h)$ is a matrix that captures the relationships among the harmonic state variables, in particular between $\mathbf{V}(h)$ and $\mathbf{I}_L(h)$, by using the circuit equations. More details about the construction of matrix $\mathbf{G}(h)$ is provided in Appendix A.

For a network that *is* fully-observable, there is no advantage to use the augmented HSE formulation in (3.5) compared to the basic HSE formulation in (3.4). However, when the network is *not* fully-observable, it is necessary to use the augmented formulation to at least include the unobservable variables in the equations of the HSE problem formulation; otherwise they cannot be even part of the analysis; because they would not show up in

any equation. Thus, for the rest of this paper, we focus on the augmented HSE problem formulation in (3.5).

Next, we consider three different scenarios: a) the case where there is one harmonic source in the network; b) the case where the are multiple harmonic sources in the network; and c) the case where the number of harmonic sources is unknown.

3.3 Physics-Aware HSE Solution: One Harmonic Source

In this section, we discuss a scenario where there is exactly one harmonic source in the network. The immediate result of this assumption is that exactly one entry in vector $\mathbf{I}_N(h)$ is non-zero; while all the other entries are zero. In other words, there is an inherent *sparsity* in the construction of vector $\mathbf{I}_N(h)$, which can be mathematically expressed as:

$$\mathbf{e}_i^\top \mathbf{I}_N(h) = 0, \quad \forall\, i \in \mathcal{N}\backslash\{k\}, \tag{3.6}$$

where k is the bus number for the location of the harmonic source; and $\mathbf{e}_i$ is a standard basis vector with all its entries being equal to zero, except for the entry at row i which is one.

Given the radial topology of the power distribution systems, one may ask: how does the inherent sparsity in vector $\mathbf{I}_N(h)$ may create sparsity in vectors $\mathbf{I}_L(h)$ and $\mathbf{V}(h)$?

Next, we answer this question by using the physical characteristics of the underlying power distribution circuit. Accordingly, we build the foundation for our proposed physics-aware HSE solution for low-observable power distribution systems.

3.3.1 Fundamental Sparsity in Radial Networks

Again Consider the power distribution feeder in Fig. 3.1. Suppose there is exactly one harmonic source in the network. Suppose the harmonic source is at bus 13. The harmonic source injects the harmonic current to the distribution feeder; accordingly, it is modeled as a current source in Fig. 3.1.

As it is shown in [11, 19, 44], and also explained in Appendix B, the injected harmonic current at bus 13 almost entirely flows through the substation and *not* through the loads. The reason is that the impedance in the Thevenin equivalent of the substation that is seen by the distribution feeder, which is marked by Z_{Thevenin} in Fig. 3.1, is much less than the impedance of the loads on the distribution feeder. Thus, almost the entire harmonic current that is injected by the harmonic source passes through the *substation connector* path, i.e., the lines that are marked in red, from bus 13 all the way up to the substation.

We can analyze the impact of injecting harmonic current by a harmonic source at any other bus in the network in a similar way, i.e., based on the substation connector path between the location of the harmonic source and the substation.

From the above physics-based observation in radial networks, together with the inherent sparsity in (3.6), we can conclude that the entries in vector $\mathbf{I}_L(h)$ that are associated with the line segments on the connector path between bus k and the substation are non-zero; while all the other entries are almost zero. In other words, the entries in $\mathbf{I}_L(h)$

that correspond to the line segments in set $\mathcal{L}_k$ are non-zero; while the entries in $\mathbf{I}_L(h)$ that correspond to the line segments in set $\mathcal{L}\backslash\mathcal{L}_k$ are zero. This can be mathematically expressed:

$$\mathbf{e}_l^\top \mathbf{I}_L(h) \approx 0, \quad \forall\, l \in \mathcal{L}\backslash\mathcal{L}_k, \tag{3.7}$$

where $\mathcal{L}_k$ is the set of all line segments that belong to the substation connector path for bus k. Note that, $\mathcal{L}_k \subseteq \mathcal{L}$.

The zero approximations in harmonic currents in (3.6) and (3.7) also have implications on nodal harmonic voltages in $\mathbf{V}(h)$. To see this, let us define $\mathcal{N}_k$ as the set of all buses that are on the substation connector path for bus k. Furthermore, for each bus i in set $\mathcal{N}\backslash\mathcal{N}_k$, let us define $p(k,i)$ as the bus that is the most downstream *parent* of bus i that belongs to set $\mathcal{N}_k$. For example, for the scenario in Fig. 3.1 with $k = 13$, we have:

$$p(13,23) = p(13,24) = p(13,25) = 3. \tag{3.8}$$

This is because bus 3 is the most downstream parent of buses 23, 24, and 25 that belongs to the substation connector path between bus 13 and the substation. From (3.7), the harmonic voltage phasor at buses 23, 24, and 25 is almost equal to the harmonic voltage phasor at bus 3. This comes from the fact that there is no harmonic current on the line between buses 3 and 23, the line between buses 23 and 24, and the line between buses 24 and 25; therefore, there is no harmonic voltage difference across buses 3, 23, 24, and 25. This leads to the following voltage approximation in the power system:

$$\mathbf{e}_i^\top \mathbf{V}(h) - \mathbf{e}_{p(k,i)}^\top \mathbf{V}(h) \approx 0, \quad \forall\, i \in \mathcal{N}\backslash\mathcal{N}_k. \tag{3.9}$$

As a result, we do *not* need to estimate all the harmonic voltage phasors in the system. Instead, we can only estimate harmonic voltage phasors at the buses that are on the sub-

station connector path for bus k. The rest of the harmonic voltage phasors are then readily obtained from the approximation in (3.9).

Summary: Based on the analysis in (3.6), (3.7), and (3.9), the total number of harmonic state variables that we need to estimate for the scenario with one harmonic source at bus k is:

$$|\mathcal{N}_k| + |\mathcal{L}_k| + 1. \tag{3.10}$$

In other words, since the total number of harmonic state variables of harmonic order h in the system is $2|\mathcal{N}| + |\mathcal{L}|$, the total number of harmonic state variables that we can readily obtain from the results in (3.6), (3.7), and (3.9) is:

$$2\,|\mathcal{N}| + |\mathcal{L}| - |\mathcal{N}_k| - |\mathcal{L}_k| - 1. \tag{3.11}$$

For example, for the scenario in Fig. 3.1, the number of state variables to estimate is $13 + 12 + 1 = 26$. The remaining 72 variables are obtained from (3.6), (3.7), and (3.9).

3.3.2 Physics-Aware MIQP Formulation

In this section, we integrate the physics-based approximations in (3.6), (3.7), and (3.9) into the formulation of the augmented HSE problem in (3.5). This is done by introducing a novel and tractable mixed-integer formulation for the HSE problem.

Let us define $\boldsymbol{b}$ as an $|\mathcal{N}| \times 1$ vector of binary variables. For each row k, the corresponding entry is 1 if the harmonic source is located at bus k; otherwise the entry is 0. From (3.6), we know that exactly one entry in $\boldsymbol{b}$ is 1 and all other entries are 0. This can be mathematically expressed as:

$$\mathbf{1}^\top \boldsymbol{b} = 1. \tag{3.12}$$

Also, from (3.6), we know that harmonic nodal injection current is zero for all the buses in $\mathcal{N}\backslash\{k\}$. We can express this sparsity pattern through the defined binary variables as:

$$-M\,\boldsymbol{b} \leq \mathbf{I}_N(h) \leq M\,\boldsymbol{b}, \tag{3.13}$$

where M is a large number. In total, there are $|\mathcal{N}|$ rows of both lower-bound and upper-bound inequalities in (3.13). From (3.13), together with (3.12), the harmonic nodal injection current is zero for all the buses in $\mathcal{N}\backslash\{k\}$, i.e., all the buses that are *not* the location of the harmonic source. For any of such buses, the corresponding row in (3.13) forms a pair of a *lower bound at zero* and an *upper bound at zero*; thus, forcing the harmonic current injection to be zero. This is done *without* knowing the location of the harmonic source in advance; because the constraints in (3.13) are defined based on the binary vector $\boldsymbol{b}$.

It is worth mentioning that, the constraints in (3.13) have no impact on the harmonic nodal injection current at the location of the harmonic source. This is because the corresponding lower bound and the corresponding upper bound would be ineffective; due to the fact that M is a large number.

In order to incorporate the binary vector $\boldsymbol{b}$ in the approximate equality constraints in (3.7) and (3.9), let us first define:

$$U = \sum_{k\in\mathcal{N}} \big|\mathcal{L}\backslash\mathcal{L}_k\big|, \qquad W = \sum_{k\in\mathcal{N}} \big|\mathcal{N}\backslash\mathcal{N}_k\big|. \tag{3.14}$$

Here, U denotes the total number of the zero approximations in the form in (3.7) for *all possible choices* for the location of the harmonic source. Similarly, W denotes the total number of the zero approximations in the form in (3.9) for *all possible choices* for the location of the harmonic source. Depending on the location of the harmonic source, i.e.,

depending on which exact entry in vector $\boldsymbol{b}$ is 1, some of these zero approximations must be used and some of them must be disregarded.

Accordingly, we can express the zero approximations in (3.7) based on the defined binary variables as follows:

$$-M\ \boldsymbol{\Psi}\ (\mathbf{1}-\boldsymbol{b}) \leq \mathbf{A}\ \mathbf{I}_L(h) \leq M\ \boldsymbol{\Psi}\ (\mathbf{1}-\boldsymbol{b}), \tag{3.15}$$

where $\boldsymbol{\Psi}$ is a matrix of size $U \times |\mathcal{N}|$; and $\mathbf{A}$ is a matrix of size $U \times |\mathcal{L}|$. In each row of matrix $\boldsymbol{\Psi}$, exactly one entry is 1, and all the other entries are zero. Similarly, in each row of matrix $\mathbf{A}$, exactly one entry is 1, and all the other entries are zero. In total, there are U rows of both lower-bound and upper-bound inequalities in (3.15). From (3.15), together with (3.12), the harmonic line current is zero for all the lines in set $\mathcal{L}\backslash\mathcal{L}_k$, i.e., for all the lines that are *not* on the connector path between the location of the harmonic source and the substation. For all such lines, the corresponding rows in (3.15) form a pair of a *lower bound at zero* and an *upper bound at zero*; thus, forcing them to be zero. This is achieved *without* knowing the location of the harmonic source in advance; because the constraints in (3.15) are directly defined based on the binary vector $\boldsymbol{b}$.

Finally, we can also express the zero approximations in (3.9) based on the defined binary variables as follows:

$$-M\ \boldsymbol{\Phi}\ (\mathbf{1}-\boldsymbol{b}) \leq \mathbf{B}\ \mathbf{V}(h) \leq M\ \boldsymbol{\Phi}\ (\mathbf{1}-\boldsymbol{b}), \tag{3.16}$$

where $\boldsymbol{\Phi}$ is a matrix of size $W \times |\mathcal{N}|$; and $\mathbf{B}$ is also a matrix of size $W \times |\mathcal{N}|$. In each row of matrix $\boldsymbol{\Phi}$, exactly one entry is 1, and all the other entries are zero. In each row of matrix $\mathbf{B}$, exactly one entry is 1, exactly one entry is -1, and all the other entries are zero. In

total, there are W rows of both lower-bound and upper-bound inequalities in (3.16). From (3.16), together with (3.12), the equality in (3.9) holds for any bus in set $\mathcal{N}\backslash\mathcal{N}_k$ for any choice of bus k as the location of the harmonic source. Just like in (3.13) and (3.15), this is achieved *without* knowing the location of the harmonic source in advance; because the constraints in (3.16) are defined based on the binary vector $\boldsymbol{b}$.

We are now ready to reformulate the HSE optimization problem as follows, where the physics-aware sparsity patterns are fully integrated into the problem formulation:

$$\underset{\mathbf{X}(h),\boldsymbol{b}}{\textbf{minimize}} \quad \left\| \begin{bmatrix} \mathbf{Z}(h) \\ \\ \mathbf{0} \end{bmatrix} - \begin{bmatrix} \mathbf{H}(h) \\ \\ \mathbf{G}(h) \end{bmatrix} \mathbf{X}(h) \right\|_2^2 \tag{3.17}$$

$$\textbf{subject to} \quad \text{Eqs. } (3.1), (3.12), (3.13), (3.15), (3.16).$$

The above optimization problem is an MIQP, where the objective function is a standard Least-Square (LS) formulation over *continuous* variables, while the constraints are linear mixed-integer. The MIQP in (3.17) can be solved by using various optimization solvers, including CVX toolbox in MATLAB [48]. Once the optimal solutions are obtained, the only non-zero entry in $\mathbf{b}$ pinpoints the host bus for the harmonic source; and $\mathbf{X}(h)$ provides us with the estimation of harmonic state variables. Therefore, the proposed HSE method not only does not need any prior information about the location of harmonic source, but also it gives us the exact host location in addition to the estimation results under the low-observability conditions.

3.4 Physics-Aware HSE Solution: Multiple Harmonic Sources

The MIQP formulation in (3.17) fully incorporates the fundamental physics-based concepts that we discussed in Section 3.3.1. However, a key assumption in (3.17) is that there is only *one* harmonic source in the network. This assumption may *not* always hold in practice. Therefore, in this section, we properly extend the proposed physics-aware HSE solution to the case where there are *multiple* harmonic sources in the network.

If each of the harmonic sources in the network has a *different* harmonic order, then we can simply solve the optimization problem in (3.17) for *each* harmonic order *separately*. In such cases, the HSE problem reduces to the same analysis as in Section 3.3. Therefore, for the rest of this section, we rather focus on the more challenging case where there exist multiple harmonic sources of the *same* harmonic order.

Throughout this section, we assume that the number of harmonic sources is known; but their locations are unknown. The case in which neither the number nor the locations of the harmonic sources are known will be discussed in Section 3.5.

3.4.1 Decomposition of the Problem

To address the case with multiple harmonic sources, we apply the *superposition theorem* from Circuit Theory [67]. We decompose the HSE problem and introduce a separate set of state variables corresponding to each harmonic source based on a separate equivalent circuit. Once the harmonic voltage phasors and the harmonic current phasors are defined separately in accordance to each individual harmonic source and its correspond-

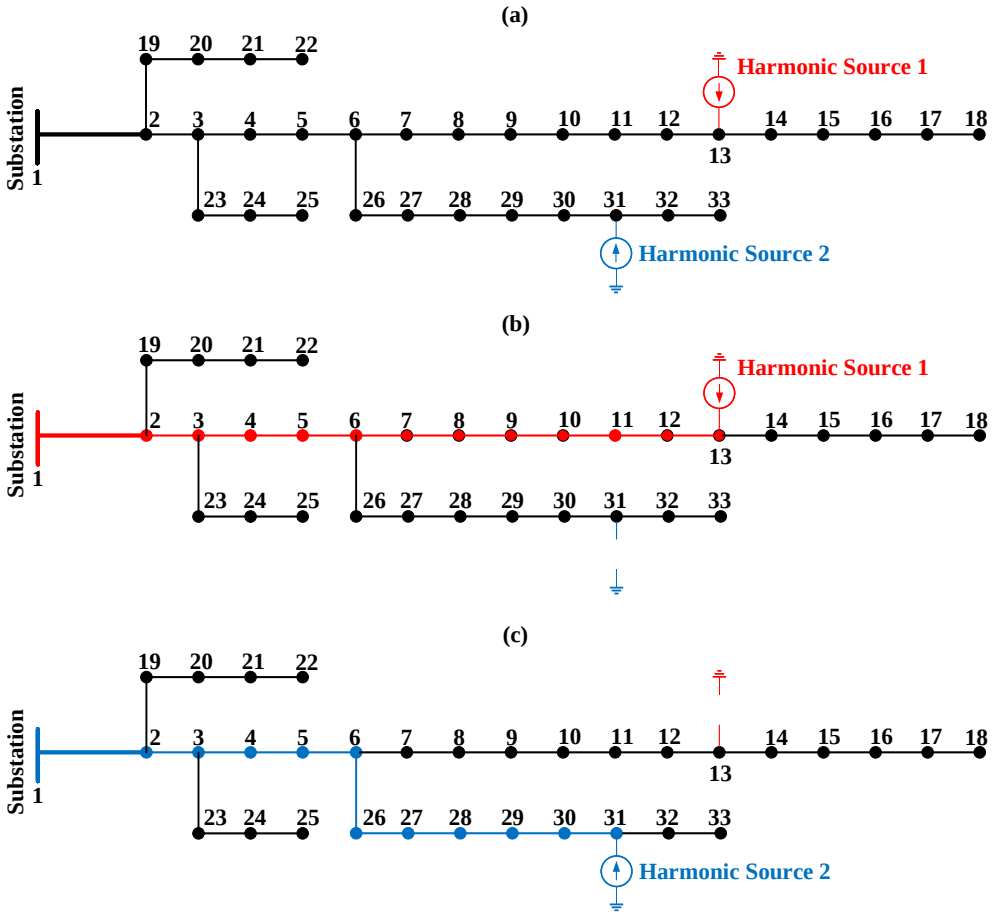

Figure 3.2: An example distribution feeder with multiple harmonic source. In practice, the harmonic current almost entirely flows through the substation.

ing equivalent circuit, we can algebraically add them together in order to obtain the overall harmonic state variables for the understudy power distribution system.

An example is shown in Fig. 3.2. First, consider the power distribution feeder in Fig. 3.2(a), which has two harmonic sources of the same harmonic order at buses 13 and 31. Each harmonic source injects a certain level of harmonic current to the network. Based on the superposition theorem, we can decompose the analysis of this circuit into two separate cases, one based on the analysis of *only* the harmonic source at bus 13; see Fig. 3.2(b), and

another one based on the analysis of *only* the harmonic source at bus 31; see Fig. 3.2(c). Similar to the discussion in Section 3.3.1, the injected current from each of the two harmonic sources flows through its associated substation connector path, as marked on Figs. 3.2(b) and (c), respectively. If we denote the vector of the state variables corresponding to the decomposed circuit for the first harmonic source by $\mathbf{X}_1(h)$ and the vector of the state variables corresponding to the decomposed circuit for the second harmonic by $\mathbf{X}_2(h)$, then from the superposition theorem, we know that:

$$\mathbf{X}(h) = \mathbf{X}_1(h) + \mathbf{X}_2(h), \tag{3.18}$$

where $\mathbf{X}(h)$ is the vector of state variables for the original circuit, i.e., the one that has multiple harmonic sources.

We can similarly break down any power distribution circuit with multiple harmonic sources to a superposition of multiple decomposed circuits; thus solving the HSE problem separately for each harmonic source; and then adding up the results. This approach is explained in details in the next subsection.

3.4.2 Extended Physics-Aware MIQP Formulation

For a given harmonic order h, suppose there are $K(h)$ harmonic sources across the distribution feeder. Let us define:

$$\mathcal{K}(h) = \big\{1, \ldots, K(h)\big\}. \tag{3.19}$$

Based on our discussion in the previous section, let us apply the superposition theorem and decompose the distribution feeder into $K(h)$ circuits such that in each of them only one of

the harmonic sources is present and the rest are eliminated. For each $\kappa \in \mathcal{K}(h)$, let $\mathbf{X}_\kappa(h)$ denote the vector of state variables for the decomposed circuit by the superposition theorem that corresponds to the κ-th harmonic source:

$$\mathbf{X}_\kappa(h) = [(\mathbf{I}_{N,\kappa}(h))^\top \ (\mathbf{I}_{L,\kappa}(h))^\top \ (\mathbf{V}_\kappa(h))^\top]^\top. \tag{3.20}$$

We can expand the summation in (3.18) to have:

$$\mathbf{X}(h) = \sum_{\kappa \in \mathcal{K}(h)} \mathbf{X}_\kappa(h). \tag{3.21}$$

Similar to (3.12), for each decomposed circuit, we know that only one harmonic source is present. Therefore, we have:

$$\mathbf{1}^T \boldsymbol{b}_\kappa = 1, \quad \forall \kappa \in \mathcal{K}(h). \tag{3.22}$$

Furthermore, similar to (3.13)-(3.16), we know that the following equations hold for each set of state variables associated with each of the decomposed circuits for each harmonic source:

$$\mathbf{I}_{N,\kappa}(h) \leq M \, \boldsymbol{b}_\kappa, \qquad \forall \kappa \in \mathcal{K}(h), \tag{3.23}$$

$$\mathbf{I}_{N,\kappa}(h) \geq -M \, \boldsymbol{b}_\kappa, \qquad \forall \kappa \in \mathcal{K}(h), \tag{3.24}$$

$$\mathbf{A} \, \mathbf{I}_{L,\kappa}(h) \leq M \, \boldsymbol{\Psi} \, (\mathbf{1} - \boldsymbol{b}_\kappa), \qquad \forall \kappa \in \mathcal{K}(h), \tag{3.25}$$

$$\mathbf{A} \, \mathbf{I}_{L,\kappa}(h) \geq -M \, \boldsymbol{\Psi} \, (\mathbf{1} - \boldsymbol{b}_\kappa), \qquad \forall \kappa \in \mathcal{K}(h), \tag{3.26}$$

$$\mathbf{B} \, \mathbf{V}_\kappa(h) \leq M \, \boldsymbol{\Phi} \, (\mathbf{1} - \boldsymbol{b}_\kappa), \qquad \forall \kappa \in \mathcal{K}(h), \tag{3.27}$$

$$\mathbf{B} \, \mathbf{V}_\kappa(h) \geq -M \, \boldsymbol{\Phi} \, (\mathbf{1} - \boldsymbol{b}_\kappa), \qquad \forall \kappa \in \mathcal{K}(h). \tag{3.28}$$

Matrices $\mathbf{A}$, $\mathbf{B}$, $\boldsymbol{\Phi}$, and $\boldsymbol{\Psi}$ do *not* have superscript κ; because they do not depend on the number of harmonic sources.

We can now MIQP formulation in (3.17) to the case with the presence of multiple harmonic sources as follows:

$$\underset{\substack{\mathbf{X}(h),\mathbf{X}_\kappa(h),\boldsymbol{b}_\kappa \\ \forall \kappa \in \mathcal{K}(h)}}{\textbf{minimize}} \left\| \begin{bmatrix} \mathbf{Z}(h) \\ \\ \mathbf{0} \end{bmatrix} - \begin{bmatrix} \mathbf{H}(h) \\ \\ \mathbf{G}(h) \end{bmatrix} \mathbf{X}(h) \right\|_2^2 \tag{3.29}$$

$$\textbf{subject to} \quad \text{Eqs. } (3.1), (3.20) - (3.28).$$

The above optimization problem incorporates all the harmonic sources into one integrated formulation. Note that, the optimization variables corresponding to all the harmonic sources are *coupled* through the constraints in (3.21); therefore, they all simultaneously affect the objective function in (3.29).

In each binary vector $\boldsymbol{b}_\kappa$, only one entry is non-zero; which pinpoints the location of the κ-th harmonic source. The solution of the optimization problem in (3.29) gives us the estimation of the state variables for the original circuit, as well as those for all the $K(h)$ decomposed circuits. Just like the problem in (3.17), the problem in (3.29) is a MIQP. Hence, it can be solved by using a commercial solver such as CVX [48].

With regards to the complexity of our method, suppose there are $K(h)$ harmonic sources of order h across the distribution feeder. The MIQP HSE formulation in (3.29) would include $K(h) \times (2 \times |\mathcal{N}| + |\mathcal{L}|)$ continuous variables (corresponding to harmonic state variables) and $K(h) \times |\mathcal{N}|$ binary variables (corresponding to the harmonic sources to be identified).

Importantly, if the binary variables are relaxed, then the MIQP optimization in (3.29) becomes a convex optimization problem. Therefore, the complexity of the method primarily depends on the number of binary variables, i.e., $K(h) \times |\mathcal{N}|$.

Algorithm 1 HSE in low-Observable distribution network with *unknown* number and location(s) of harmonic source(s)

Set threshold ζ.

Set $\mathbf{X}^*(h) = \mathbf{0}$.

Set $\mathcal{K}^*(h) = \{\}$.

$K = 1$ to $|\mathcal{N}| - 1$ Solve Problem (3.29) to obtain $\mathbf{X}(h)$.

condition (3.30) holds $\mathbf{X}^*(h) = \mathbf{X}(h)$;

$\mathcal{K}^*(h) = \{1, \ldots, K\}$.

break;

3.5 Physics-Aware HSE Solution: Unknown Number of Harmonic Sources

So far, we have assumed that the number of harmonic sources, i.e., $K(h)$ is known to us. The final step to complete our design in this paper is to relax such assumption. In this section, we assume that $K(h)$ is *not* known. Instead, it needs to be estimated. This can be done by using a novel algorithm, as shown in Algorithm 1. This algorithm is based on conducting an exhaustive search. The key in this algorithm is the *for loop* from Line 4 to Line 12. At first, we assume that there is only one harmonic source in the system, i.e., $K = 1$, and we solve the HSE problem in (3.29). Next, we set $K = 2$ and solve (3.29) again. Every time we do so, a new non-zero entry is obtained in vector $\mathbf{I}_N(h)$, while the value and the location of the previous non-zero entries may also change.

What matters to us in this exhaustive search is the value of the smallest non-zero entry in the vector of harmonic nodal injection current phasors, i.e., $\mathbf{I}_N(h)$. Let $\mathbf{I}_N^{\neq 0}(h)$ denote the vector which includes only the non-zero entries of vector $\mathbf{I}_N(h)$. In every iteration that we solve the HSE problem, we check to see if the following condition holds:

$$\min\left\{\mathbf{I}_N^{\neq 0}(h)\right\} \geq \zeta, \tag{3.30}$$

where ζ is a predefined threshold which is selected based on the smallest harmonic current magnitude that we are concerned about in practice for nodal injection by a harmonic source. If the inequality in (3.30) does *not* hold, then it means that we have already passed the actual number of harmonic sources; and the value of K in the *previous* iteration is the true number. Once the algorithm ends it returns the number of harmonic sources as well as the ultimate results for harmonic state estimation.

As a special case, if there is *no* harmonic source in the network, then the algorithm ends *without* changing the initial values for $\mathbf{X}^*(h)$ and $\mathbf{K}^*(h)$. Accordingly, the outcome of Algorithm 1 is correct even under such special case.

3.6 Placement of H-PMUs

In this paper, we assume that only very few H-PMUs are available. Therefore, low-observability is the primary challenge, *regardless* of *where* the H-PMUs are located. Thus, sensor placement is *not* the focus of this paper. Instead, we assume that the H-PMUs are already installed at very few locations; and we rather focus on solving the HSE problem to cope with the low-observability issues. It should be added that, in this work, H-PMUs are assumed to be installed at only $15\% - 25\%$ of the buses. For instance, for the IEEE

33-bus test network that we will discuss in Section VII-D, only six buses (i.e., only 18% of the buses) are assumed to have H-PMUs.

Nevertheless, in this section, we provide some discussions on the subject of sensor placement to serve as a supplementary insight. First, we discuss the intuitive importance of certain locations to install H-PMUs on a radial topology. Next, we provide an algorithm to select the locations of the H-PMUs.

3.6.1 Intuitive Importance of Certain Buses to Host H-PMUs

Let us again consider the IEEE 33-bus test network. We can distinguish *three groups* of buses, as marked on Fig. 3.3: 1) The buses that are circled in red, which include the substation and all the terminal buses, i.e., buses 1, 18, 22, 25, and 33. 2) The buses that are circled in blue, which are at the head of laterals, i.e., buses 2, 3, and 6. 3) The rest of the buses.

The buses in Group 1, i.e., those that are circled in red, are particularly beneficial to host H-PMUs. The intuitive reason is that, if we place H-PMUs at the buses in Group 1, then *every* bus in the system is monitored by at least a pair of an *upstream* sensor and a *downstream* sensor. The advantage of such dual monitoring has been reported also in prior studies, e.g., in [68]. Further, as we will see in a case study in Section 3.7.6, moving H-PMUs away from the buses in Group 1 leads to degradation in the HSE performance, depending on how far we move the H-PMUs away from the buses in Group 1.

The buses in Group 2, i.e., those that are circled in blue, are also (to a lesser extent) beneficial to host H-PMUs. For example, by placing an H-PMU at bus 6, we can

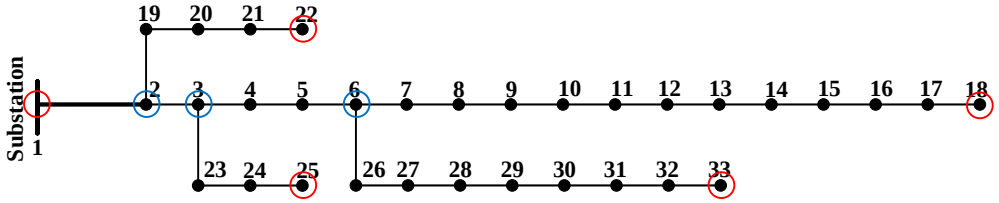

Figure 3.3: Three groups of buses on a radial feeder: 1) the buses that are circled in red, 2) the buses that are circled in blue, and 3) the rest of the buses.

enhance the *upstream* monitoring of the buses on two major branches of the radial network topology, i.e., for buses 7 to 18 on the main as well as for buses 26 to 33 on a lateral; while we also enhance the *downstream* monitoring of buses 2 to 5.

From the above intuitive explanations, and given the fact that our focus in this paper is on low-observable power networks with very few H-PMUs, we expect that the choices of the H-PMUs should include the buses in Group 1 and possibly a few buses in Group 2. Nevertheless, the main challenge remains to be the issue of low-observability in the system.

3.6.2 H-PMU Placement based on Algorithm

Further to the intuitive approach in Section VI-A, next, we provide an algorithm to choose the locations of H-PMUs based on the desired number of H-PMUs. This algorithm is provided to make the paper self-sufficient. Please refer to the very rich literature in this field, such as in [60, 61, 62, 63], for more details.

In the proposed sensor placement algorithm, we start from the case where *all* buses are equipped with an H-PMU, i.e., we start with the hypothetical case where the power distribution network has full observability. Then, in every iteration, we seek to remove

one of the H-PMUs such that we experience the lowest decline in the accuracy of the proposed HSE method after solving the optimization problem in (3.17). Here, we examine the hypothetical presence of the harmonic source at each bus and consider the *average* of the resulting MSE values. After we remove one H-PMU, we repeat this process to remove H-PMUs one by one, until we reach the desired number of installed H-PMUs. Please note that, due to the radial topology of the network, it might happen in some iterations that removing an H-PMU from a group of neighboring buses leads to an *equal* amount of decline in the MSE. In that case, one can remove the H-PMU from either one of those buses. In such rare cases, instead of removing one of the identified buses randomly, we rather follow our intuitive discussion in Section 3.6.1 and we give the priority to keep the H-PMUs at buses in Group 1 over Group 2, and Group 2 over Group 3. The summary of the above process is shown in Algorithm 2.

3.7 Case Studies

In this section, we examine different case studies based on the IEEE 33-Bus test network [49]. We run the harmonic power flow in the Open Distribution System Simulator (OpenDSS) [50], and then we use CVX toolbox with MOSEK solver [48] in MATLAB to solve the HSE optimization problem in (3.29) and to execute the steps in Algorithm 1.

Unless stated otherwise, we assume that six H-PMUs are installed on the network and measure the harmonic nodal voltage phasors and the harmonic line current phasors.

The placement of the H-PMUs is done by Algorithm 2, where the desired number of H-PMUs is $P = 6$. Accordingly, H-PMUs are installed at buses 1, 6, 18, 22, 25, and 33.

Algorithm 2 Placement of H-PMUs

1: The desired total number of available H-PMUs is P.

2: Initially, place H-PMU at every node, i.e., $\mathcal{M} = \mathcal{N}$

3: Set $\mathcal{M}^* = \{\}$

4: ***for*** $m = 1$ to $|\mathcal{N}| - P$ ***do***:

5: minMSE = $1e3$

6: $\mathcal{F} = \{\}$

7: **for** $i \in \mathcal{M}/\mathcal{M}^*$ **do**:

8: Remove H-PMU at bus i and Solve Problem (3.17).

9: **if** MSE <minMSE **then**

10: minMSE = MSE;

11: $\mathcal{F} = \{\text{i}\}$

12: **end if**

13: **end for**

14: Set $\mathcal{M}^* = \mathcal{M}^* \cup \mathcal{F}$

15: **end for**

16: Return $\mathcal{M} - \mathcal{M}^*$

We assume that up to five harmonic sources may exist on the power distribution feeder, and they may inject harmonic currents with harmonic orders $h = 3$, 5, and 7. The magnitude of the harmonic source at a bus is assumed to be up to 30% of the default load at that bus in the IEEE 33-Bus test feeder.

3.7.1 Performance Comparison

We compare the performance of our method with two other methods. We choose the methods in [37] and [39] for the purpose of performance comparison. The method in [37] is based on some popular sparse recovery techniques. It works by considering the nodal injection currents as the vector of state variables. Sparse recovery is done by conducting an ℓ_1-norm minimization. Therefore, this method is inherently designed to solve the HSE problem under the low-observability condition without the need for making any modifications. As for the method in [39], it is based on Singular Value Decomposition (SVD). It has some structural characteristics which can be used to solve an undetermined system of equations. This method addresses *low-observability* by examining singular values and the null space vectors of the measurement matrix.

As the metric for performance comparison, we use the Mean Square Error (MSE) in the HSE results. Since the magnitudes of the harmonic voltage phasors are different from the magnitudes of the harmonic current phasors, we calculate the MSE for each type of harmonic variables separately. Thus, we provide separate results for MSE V and MSE I.

The results are shown in Table 3.1. Here the harmonic source is at harmonic order $h = 3$ and the magnitude of the injected harmonic current is 30% of the default load of the bus where the harmonic source is located. As we can see, the MSE for both voltage and current is significantly lower for the proposed method in comparison with the methods in [37] and [39]. Of course, as we increase the number of harmonic sources, the MSE increases in all three methods. However, in all cases, the proposed physics-aware method performs drastically better.

Table 3.1: Performance comparison between different HSE methods

Method	K = 1		K = 2		K = 3		K = 4		K = 5	
	MSE V	MSE I	MSE V	MSE I	MSE V	MSE I	MSE V	MSE I	MSE V	MSE I
Proposed Method	0.0156	0.0019	0.8578	0.2447	0.9714	0.1383	1.7510	0.2646	25.226	9.948
[37]	201.72	4.202	408.06	13.21	971.04	20.922	1790.1	41.176	1993.2	63.66
[39]	202.21	8.71	417.33	31.89	1935.31	43.78	1879.47	78.45	2007.9	125.6

Another comparison between the performance of the proposed method and those of [37] and [39] is done is Fig. 3.4. Here we examine the MSE V for each of the three methods versus the location of a single harmonic source. The harmonic source is at harmonic order $h = 3$, and the magnitude of the injected harmonic current is 10% of the default load at each bus where the harmonic source is located. As it can be seen in Fig. 3.4, the proposed method demonstrates a much lower MSE in comparison with the works in [37] and [39].

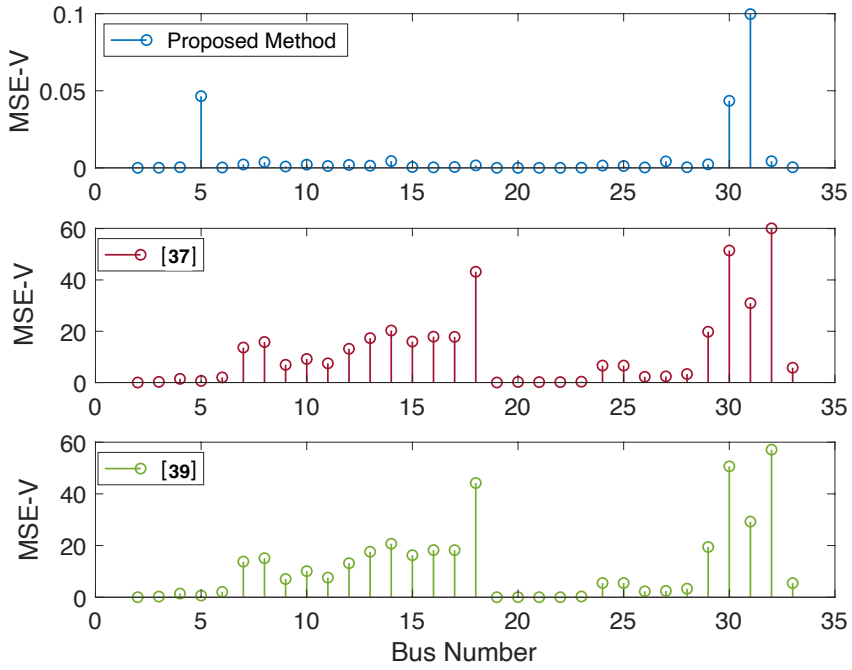

Figure 3.4: MSE in estimating harmonic voltage phasors at all buses, for three different methods, versus the location of the harmonic source. The number of harmonic sources is $K = 1$. The harmonic order is $h = 3$.

3.7.2 Harmonic Source Location Identification

Although the focus in this paper is on harmonic state estimation, it is worth to also compare our proposed method with the existing methods that are designed to identify the location(s) of harmonic source(s). In any such comparison, we would utilize only a subset

of the strengths of our proposed method. Clearly, not every HSE method can also identify the unknown location(s) and the unknown number of the harmonic source(s). However, the approach in this paper *does* provide the number and the location(s) of the harmonic source(s) as a *bi-product* of the proposed physics-aware MIQP HSE method. Therefore, making such comparison could be insightful.

In this case study, we compare the average error in identifying the location(s) of harmonic source(s) of the proposed method versus the method in [41], which is designed to identify the location(s) of the harmonic source(s). The harmonic source location identification method in [41] is based on the concept of compressed sensing. The results are shown in Fig. 3.5. As the number of harmonic sources increases, it causes degradation in the performance of both methods. However, the proposed HSE method demonstrates a better performance in all scenarios. Of course, unlike our proposed method, the method in [41] does *not* also solve the harmonic state estimation problem, as it is *not* designed to do so.

3.7.3 Unknown Number and Location(s) of Harmonic Source(s)

In this section, we investigate the performance of Algorithm 1 in correctly estimating the *number* of harmonic sources as well as the *location(s)* of the harmonic sources.

Suppose there are four harmonic sources at buses 14, 21, 24, and 29. All harmonic sources are at the same harmonic order, where $h = 3$. We assume that neither the number nor the locations of the harmonic sources are known.

Table 3.2 shows several details about the operation of Algorithm 1 for the above

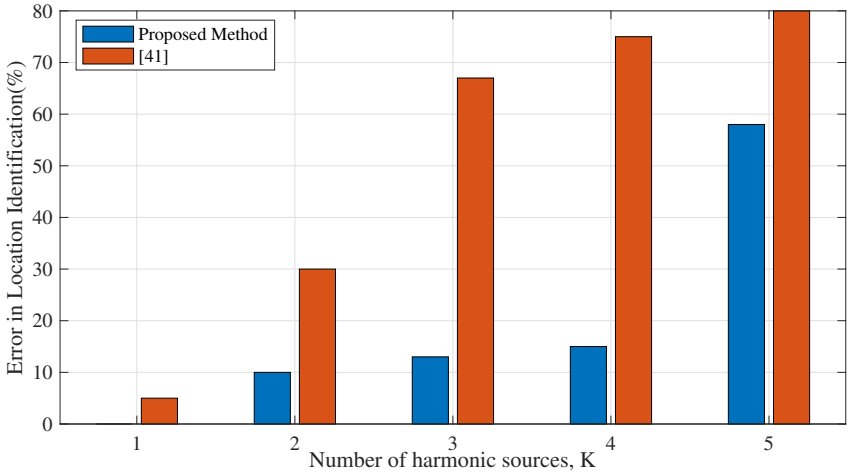

Figure 3.5: Error in location identification of the harmonic source(s).

scenario. At each step of the *for loop* in Algorithm 1, this table shows several details about the internal parameters in the algorithm. The first column denotes the value of parameter K. The second column denotes the optimal objective value of the optimization problem in (3.29). The third column shows the entries in vector $\mathbf{I}_N^{\neq 0}(h)$, i.e., the non-zero entries in vector $\mathbf{I}_N(h)$. The number in bold is the entry that has the smallest amount, i.e., the entry that is corresponding to the condition in (3.30). The fourth column shows the current list of buses in set $\mathcal{K}^*$. The number in bold is the bus number that is corresponding to the condition in (3.30). The fifth column indicates whether condition (3.30) holds; 'Yes' means condition (3.30) holds; and 'No' means condition (3.30) does not hold. Parameter ζ in (3.30) is set to 0.01.

Per Algorithm 1, we continue incrementing K for as long as condition (30) holds. Accordingly, the highest value of K for which condition (30) holds gives us the number of harmonic sources in the network. For the example, in Table 3.2 , the number of harmonic

sources is obtained as $K = 4$, which is correct. If we consider $\mathcal{K}^*(h)$ at the row corresponding to $K = 4$, it gives us the locations of all harmonic buses:

$$\mathcal{K}^*(h) = \{14, 21, 24, 29\}, \tag{3.31}$$

which is indeed correct; because the harmonic sources are indeed at buses 14, 21, 24, and 29. Notice that, for the last row in Table 3.2, that is corresponding to $K = 5$, bus 18 is *not* a correct location for a harmonic source. Its corresponding value in vector $\mathbf{I}_N^{\neq 0}(h)$ is 0.0054, which is *less* than $\zeta = 0.01$; hence, the condition in (3.30) does *not* hold at $K = 5$.

It is worth mentioning that, the optimal objective value, i.e., the value in the second column in Table 3.2, is non-increasing in terms of parameter K; it cannot increase as we increase K.

3.7.4 Increasing the Number of Harmonic Sources

Recall from Table 3.1 that increasing the number of harmonic sources (of the same harmonic order) makes the HSE problem more challenging. It is very challenging to solve the HSE problem when 1) there are several harmonic sources in the network, 2) the number of the harmonic sources is unknown, 3) the locations of the harmonic sources is unknown, and 4) we have only a few sensors deployed on the network. However, as we will show in this section, the performance of Algorithm 1 can improve by slightly increasing the number of H-PMUs.

Here, we examine a total of 100 random scenarios, where the randomness is with respect to the locations and the magnitudes of the harmonic sources. Our goal is to examine the percentage of the harmonic sources whose locations are identified correctly (or almost

Table 3.2: Performance of Algorithm 1 in Identifying the Locations of Harmonic Sources at Buses 14, 21, 24, 29

K	Optimal Objective Value	$\mathbf{I}_N^{\neq 0}(h)$	Identified Buses in $\mathcal{K}^*(h)$	Condition (3.30) Holds
1	49.031	[**15.6116**]	4	Yes
2	22.048	[5.5396, **2.8066**]	9,**24**	Yes
3	15.636	[2.841, 3.2957, **1.3907**]	13,30,**24**	Yes
4	0.282	[2.4905, **0.5127**, 3.2778, 1.6933]	14,**21**,24,29	Yes
5	0.236	[2.4767, **0.0054**, 0.5127, 3.2791, 1.6964]	14,**18**,21,24,29	**No**

correctly). The results are shown in Fig. 3.6. In each bar, the dark portion indicates the cases where the exact bus is identified while the light portion indicates the cases where the *immediate neighboring* bus is identified. Therefore, the length of each bar indicates the percentage of the the harmonic sources whose locations are identified either exactly or by only one bus difference.

First, consider the case with the default number of H-PMUs, i.e., when there are six H-PMUs in the system; one at the substation and the others at buses 6, 18, 22, 25, and 33. As we can see, the performance of Algorithm 1 is generally acceptable when K is 1, 2, 3, or 4. However, the performance drops when K is 5. Next, consider the case where the number of H-PMUs is seven. The 7th H-PMU is installed at bus 14. As we can see, the performance of Algorithm 1 improves significantly. In particular, when K is 5, the percentage of the harmonic sources whose locations are identified correctly increases to 65% (exact bus) and 83% (exact or neighboring bus). Finally, consider the case where the number of H-PMUs is eight. The 8th H-PMU is installed at bus 29. As we can see, the performance of Algorithm 1 further improves. In particular, when K is 5, the percentage of the harmonic sources whose locations are identified correctly further increases to 72% (exact bus) and 85% (exact or neighboring bus).

From the results in Fig. 3.6, we can conclude that, as the number of harmonic sources increases, we would need more H-PMUs to be installed in the system in order to maintain high accuracy in the harmonic state estimation results.

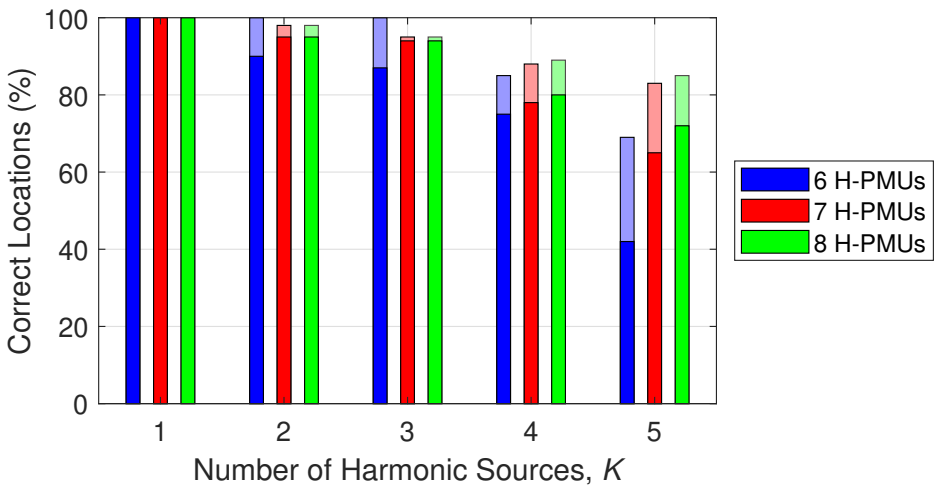

Figure 3.6: The impact of increasing the number of H-PMUs on improving the performance of Algorithm 1 in identify the locations of the harmonic sources as we increase the number of harmonic sources in the network. In each bar, the dark portion indicates the cases where the exact bus is identified while the light portion indicates the cases where the neighboring bus is identified.

3.7.5 Increasing the Harmonic Order

To investigate the effect of harmonic order on the accuracy of the proposed HSE method, we perform a sensitivity analysis based on the harmonic order h, and with respect to different number of harmonic sources K. We compare the results of our method with those of the methods in [37] and [39]. To have a consistent comparison, we assume that the magnitude of the harmonic injection current for different harmonic orders is the same. The magnitude of each harmonic source is 10% of the default load at the bus where the harmonic source is located. The results for the MSE of harmonic nodal voltage phasors and the MSE of harmonic line current phasors are shown in Table 3.3. As we can see, the proposed method demonstrates a drastically better performance compared with [37] and [39].

Table 3.3: Performance Under Different Harmonic Orders

K	h	MSE V			MSE I		
		Proposed Method	[37]	[39]	Proposed Method	[37]	[39]
1	3	0.0017	1.25	7.02	0.00025	0.94	0.83
	5	0.0046	1.96	17.3	0.00028	1.17	1.29
	7	0.0089	2.63	32.9	0.00035	1.37	1.94
2	3	0.0030	3.91	18.3	0.00037	1.65	2.20
	5	0.0077	6.28	40.8	0.00049	2.10	3.39
	7	0.0153	8.35	100	0.00060	2.43	4.36
3	3	0.0052	6.40	30.9	0.00077	2.25	3.42
	5	0.0323	10.1	74	0.00858	2.84	5.29
	7	0.1075	13.1	134	0.01467	3.28	6.81
4	3	0.0718	11.9	101	0.00970	3.20	4.80
	5	0.0917	19.1	141	0.01050	4.08	7.40
	7	0.1590	24.7	202	0.02150	4.60	10.1

3.7.6 Impact of Changing the Location of H-PMUs

As it was mentioned in Section 3.1.2, sensor placement is beyond the scope of this paper. Nevertheless, it is interesting to examine the sensitivity of our proposed method to changing the location of an H-PMU. Thus, in this section, we examine the results when we change the location of the H-PMU that is at bus 33. Here, we move the sensor to every bus on an entire lateral that includes buses 26 to 33. The results are shown in Fig. 3.7. As we can see, the performance of the method, i.e., the MSE index, remains almost unchanged as we move up to three buses away from the default location of the sensor at the end of the lateral. However, if we move away even further, then we gradually start experiencing degradation in the performance. We can conclude that, the best option is to stick to the typical placement of the sensors as in the aforementioned default setting. Nevertheless, we can see that the proposed method is not very sensitive to the exact location of the H-PMUs, and it may cope with slight changes in the location of the sensors.

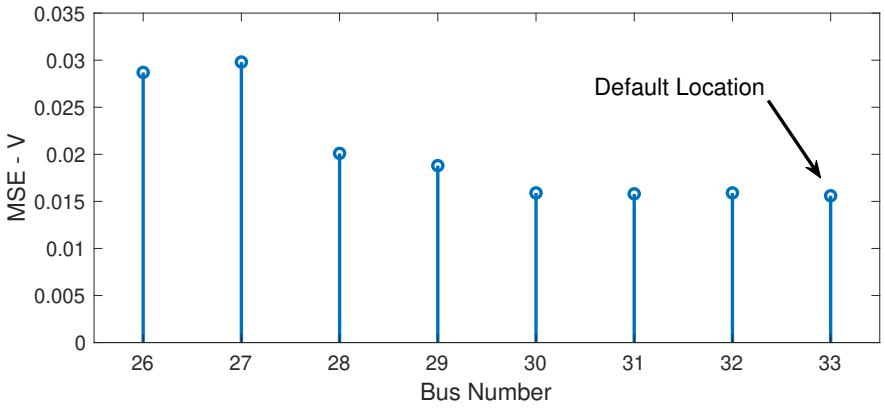

Figure 3.7: The impact of changing the location of one of the H-PMUs.

3.7.7 Impact of Unbalanced Operation

Next, we study the impact of having unbalanced phases on the performance of the proposed HSE method. In this case study, we examine a larger power distribution network, namely the IEEE 123 bus test system [69]. The majority of the loads in this test system are single phase loads that are on different phases. There are also multiple unbalanced three-phase loads with Wye connections. Many of the laterals in this network are very small. We aggregate the loads on any such small lateral as a single load point, as shown in red in Fig. 3.8. We assume that there are only four H-PMUs available, one at the substation and three at buses 95, 197 and 250. These H-PMUs provide *three-phase* harmonic voltage phasor measurements and *three-phase* harmonic line current phasor measurements. The harmonic source is at harmonic order $h = 3$ and the magnitude of the injected harmonic current is 30% of the default load at the bus where the harmonic source is located.

The results of applying the proposed HSE method are shown in Table 3.4. By comparing the results in this table and those in Table 3.1, we can see that the performance

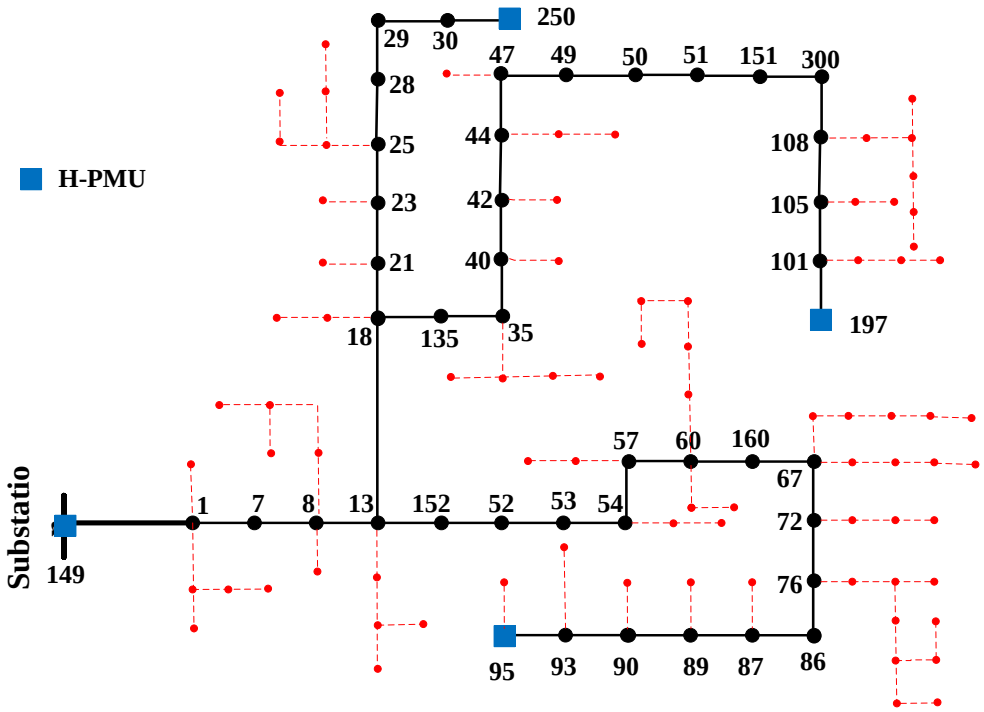

Figure 3.8: An example three-phase distribution feeder with unbalanced loads. Four H-PMUs are available at buses 95, 149, 197, and 250.

Table 3.4: Performance in an unbalanced network

K	MSE V	MSE I
1	0.0183	0.0042
2	0.9174	0.2315
3	1.1289	0.1507
4	2.3154	0.4538
5	29.258	12.743

of the proposed method remains satisfactory despite the phase unbalance in the system. This is because the unbalanced operation of the power distribution system does not change the nature of the problem, such as the characteristics of the substation connector path or the inherent linearity in the equations that directly comes from the Ohm's law. The proposed HSE method works well whether or not the network is balanced.

3.7.8 Performance in the Presence of DERs

In this Section, we evaluate the performance of our method in the presence of distributed energy resources (DERs). The results are shown in Table 3.5. Here, we assume that five DERs are at buses 5, 15, 20, 24, and 29. We consider different scenarios for different number of harmonic sources. All harmonic sources are at harmonic order $h = 3$ and the magnitude of the injected harmonic current is 30% of the default load at the bus where the harmonic source is located.

As we can see in Table 3.5, our method demonstrates similar accuracy as the previous case, where there were no DERs, such as in the results in Table 3.1. The reason is that, the presence of DERs does *not* impact the sparsity patterns that we extracted in Section 3.3. Also, it is worth mentioning that DERs may cause reverse power flow on the fundamental component of the current [19]; however, our focus in this study is rather on the harmonic components, not the fundamental component.

Table 3.5: Performance in the Presence of DERs

	K =1	K = 2	K = 3
MSE - V	0.0158	0.8913	0.9937
MSE - I	0.0025	0.2562	0.1443

3.7.9 Validation of the Superposition Theorem

We end the case studies by directly examining and validating the application of the superposition theorem in our proposed HSE method. Same as in Section 3.7.3, suppose there are four harmonic sources at buses 14, 21, 24, and 29.

For the purpose of this validation task, we run the harmonic power flow for four different cases. In each case, exactly one of the four harmonic sources is assumed to be connected to the network, while the remaining three harmonic sources are disconnected. Furthermore, we also separately run the harmonic power flow for the case that *all four* of the harmonic sources are connected to the network.

Let us denote the vector of the harmonic line current phasors corresponding to the first four cases by $\mathbf{I}_{L,1}$, $\mathbf{I}_{L,2}$, $\mathbf{I}_{L,3}$, and $\mathbf{I}_{L,4}$. They are corresponding to the simulation of the four cases with individual harmonic sources, i.e., when the only harmonic source in the network is at bus 14, at bus 21, at bus 24, and at bus 29, respectively. If the superposition theorem holds, then the following summation:

$$\mathbf{I}_{L,1} + \mathbf{I}_{L,2} + \mathbf{I}_{L,3} + \mathbf{I}_{L,4}, \tag{3.32}$$

would closely match $\mathbf{I}_L$ which is the harmonic current phasor corresponding to the case where all four harmonic sources are connected to the network. This issue is validated in Fig. 3.9. As we can see, there is almost a perfect match between the summation in (3.32), which is the outcome of applying the superposition theorem, and the actual simulation results with the simlultanous presence of all four harmonic sources.

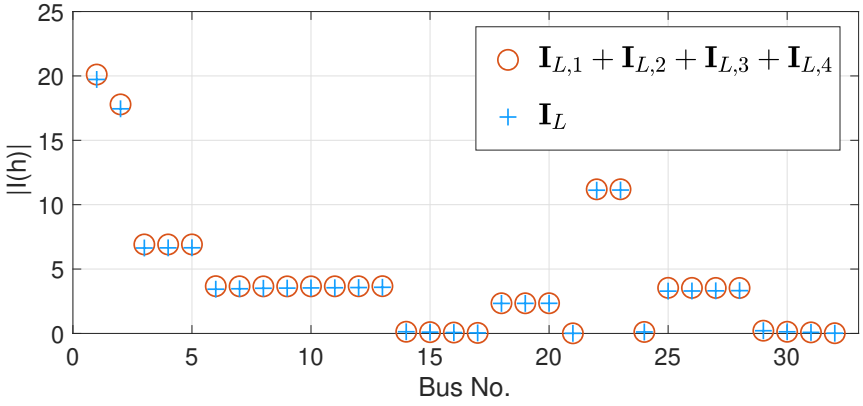

Figure 3.9: An illustrative example to validate the superposition theorem for the harmonic state variables. There are four harmonic sources on the network.

Chapter 4

Event Signatures in H-PMU Measurements: An Information-Theoretic Analysis of Real-World Data

4.1 Introduction

4.1.1 Background and Motivations

Data from Phasor Measurement Units (PMUs) have been widely used in recent years to detect, characterize, identify, and classify *events* in power systems. An event in this field is defined broadly and may refer to load switching, capacitor bank switching, connection or disconnection of distributed energy resources, inverter malfunction, momentary oscillations, a minor fault, a signature for an incipient fault, etc. Analysis of events has major applications in power system situational awareness [70, 71, 72], equipment condition monitoring [73, 74, 75], cyber-security [76], and modeling power system dynamics [77, 78].

Traditionally, PMUs provide phasor measurements based on the *fundamental* component of voltage or current. However, the fundamental phasor measurements may *not* fully capture the rich information content that is embedded in the changes that occur in voltage and current during an event.

This area has recently received a boost with the development of *Harmonic Phasor Measurement Units* (H-PMUs), which are a new class of smart grid sensors. H-PMUs can provide not only the phasor measurements for the fundamental component (same as in the traditional PMUs), but also the phasor measurements for the harmonic components. We refer to [79, 15, 80, 16, 17] for more details about the recent developments in the field of H-PMUs. Thus, in this paper, we seek to examine the *event signatures* as captured not only in the fundamental phasor measurements but also in the harmonic phasor measurements.

Throughout this paper, we use real data from a test site in California. An example is shown in Fig. 4.1. The measurements are three-phase, but only one phase is shown here.

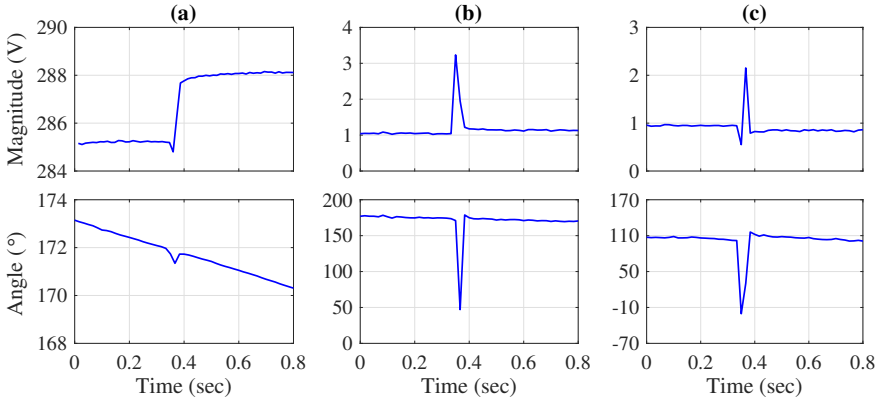

Figure 4.1: Signatures of an event in: (a) fundamental phasor measurements, (b) third harmonic phasor measurements, (c) fifth harmonic phasor measurements.

Fig. 4.1(a) shows the signature of an event in the fundamental phasor measurements. Figs. 4.1(b) and (c) show the signatures of the *same* event in the third and the fifth harmonic phasor measurements, respectively. These signatures demonstrate important features, both in transient changes and in steady-state changes, as well as both in magnitude and in phase angle.

The type of harmonic phasor signatures that are shown in Figs. 4.1(b) and (c) are currently unexplored as they have *not* been used in the literature to study power system events. However, when available, the further information that is provided about an event by these additional phasor measurements can significantly enhance our ability to make inferences.

4.1.2 Related Work

PMU measurements have been widely used for the analysis of power system events. Various methods have been developed for examining the event signatures in the fundamental

phasor measurements, such as to do event detection [71], event location identification [81], and event type classification [82, 83].

As for the literature on harmonic phasor measurements, the focus so far has *not* been on the analysis of event signatures. It has been rather on the following three general categories. First, there are studies that focus on the design of H-PMU devices and the signal processing methods to accurately obtain the harmonic phasors, such as by using matrix pencil method [84]. Second, there are studies that seek to identify the sources of harmonics in power systems, such as based on Harmonic State Estimation (HSE) [24, 85]. This line of work also includes methods to assess the daily harmonic variations in power systems [86]. Importantly, the work in this category is only concerned with the *steady state* analysis of harmonics. It is *not* concerned with the analysis of power system events. Third, there are studies that focus on other (less traditional) applications of harmonic phasor measurements, such as in topology identification [19], fault location identification [87, 88], and detection of wide-band oscillations in power systems [89].

There are also studies that investigate which certain harmonic orders are created as the result of which certain physical phenomena; albeit with focus on steady-state harmonics. For example, the third harmonic is common when there are issues in three-phase systems without a neutral, while the fifth harmonic can be due to the saturation in the transformers' cores [90].

Different from the above-mentioned literature, in this paper, we take a rather unique approach to harness the additional information provided by harmonic phasor signatures to better analyze power system events. The only other study that has touched on a

similar idea is the recent work in [91], in which Graph Learning is used to investigate events. In [91], the main focus is still on fundamental phasors; yet an example is presented for the case where some harmonic phasor measurements are included in the analysis. Notably, the example in [91] was based on *computer simulations*, and *not* real-world data. Here, we take a new and more fundamental approach by using information theory and by analyzing real-world data.

4.2 Problem Statement

The purpose of this study is to investigate the hypothesis that the event signatures in harmonic phasor measurements can uncover some significant insights about power system events, that are *not* captured by the event signatures in the conventional fundamental phasor measurements. Suppose a conventional PMU provides the following vectors of *fundamental* voltage and current phasor measurements during an event:

$$\mathbf{V}_1 \angle \boldsymbol{\theta}_1, \mathbf{I}_1 \angle \boldsymbol{\phi}_1, \tag{4.1}$$

where

$$\begin{aligned} \mathbf{V}_1 &= \left[\, V_1[1] \;\ldots\; V_1[n] \,\right]^T, \;\; \mathbf{I}_1 = \left[\, I_1[1] \;\ldots\; I_1[n] \,\right]^T \\ \boldsymbol{\theta}_1 &= \left[\, \theta_1[1] \;\ldots\; \theta_1[n] \,\right]^T, \;\; \boldsymbol{\phi}_1 = \left[\, \phi_1[1] \;\ldots\; \phi_1[n] \,\right]^T \end{aligned} \tag{4.2}$$

are the time-series of the magnitude of the fundamental voltage phasor, the magnitude of the fundamental current phasor, the phase angle of the fundamental voltage phasor, and the phase angle of the fundamental current phasor, respectively. Parameter n is the number of phasor measurements that are recorded in the window of time series that captures each event.

Next, suppose we replace the conventional PMU with an H-PMU. In addition to providing the fundamental voltage and current phasor measurements in (4.2), the H-PMU can also provide the following complex-valued vectors of *harmonic* voltage and current phasor measurements during the event:

$$\begin{aligned} &\mathbf{V}_2\angle\boldsymbol{\theta}_2, \mathbf{V}_3\angle\boldsymbol{\theta}_3, \ldots, \mathbf{V}_m\angle\boldsymbol{\theta}_m \\ &\mathbf{I}_2\angle\boldsymbol{\phi}_2, \mathbf{I}_3\angle\boldsymbol{\phi}_3, \ldots, \mathbf{I}_m\angle\boldsymbol{\phi}_m \end{aligned} \tag{4.3}$$

Here, the harmonic phasors are reported by the H-PMU up to harmonic order m. In practice, the H-PMU may not report all the harmonic phasors. For example, it may only report the third and the fifth harmonics. Or it may only report the two most dominant harmonics; see [11, Section 4.5]. Furthermore, the H-PMU may or may not report both the harmonic voltage phasors and the harmonic current phasors. For example, for the phasor measurements in Fig. 4.1, the H-PMU only reported $\mathbf{V}_3\angle\boldsymbol{\theta}_3$ and $\mathbf{V}_5\angle\boldsymbol{\theta}_5$, in addition to reporting $\mathbf{V}_1\angle\boldsymbol{\theta}_1$.

It is clear that an H-PMU provides *more data* than a conventional PMU. However, our question is on whether (and to what extent) the event signatures in the harmonic phasor measurements in (4.3) provide *more information* than the event signatures in the fundamental phasor measurements in (4.2), *as far as the analysis of the power system events is concerned*. The presence and the extent of such additional information can depend on the type of the event that is captured and the order of the harmonic phasor that is measured. We seek to address this open problem by using concepts from information theory.

The nature of this study is inherently *data-driven*. Therefore, we leverage a real-world dataset from a substation in California. The measurements are made at the secondary side of a 69 kV to 12.47 kV transformer that supplies a power distribution feeder. The

dataset covers one whole year of power system events, from March 1, 2022 to February 28, 2023. A total of 2400 events were recorded during this period. All events are three-phase and often unlabeled. For each event, the voltage and current phasors are recorded, both at the fundamental and harmonic frequencies.

4.3 Methodology: An Information Theoretic Approach

4.3.1 Entropy and Information Content

We commence our proposed approach by introducing the concept of *entropy*, which is the foundation of information theory [92]. For a random variable, entropy measures the inherent uncertainty or randomness of its outcomes. For a discrete random variable A, entropy $H(A)$ is defined as:

$$H(A) = -\sum_{a \in \mathcal{A}} P_A(a) \log P_A(a), \tag{4.4}$$

where P_A is the probability mass function of discrete random variable A over its support set $\mathcal{A}$, which is the set of all possible values that A can take with a non-zero probability.

Given another discrete random variable B, the notion of conditional entropy can be similarly defined as [93]:

$$H(A|B) = -\sum_{a \in \mathcal{A}} \sum_{b \in \mathcal{B}} P_{A,B}(a,b) \log \left(\frac{P_{A,B}(a,b)}{P_B(b)} \right), \tag{4.5}$$

where $P_{A,B}$ is the joint probability mass function of A and B. The conditional entropy measures the average residual uncertainty about variable A once variable B has been observed.

Together, the above two concepts lay the groundwork for the definition of Mutual Information (MI), a measure of the reduction in uncertainty about random variable A when random variable B is observed [92], or in other words, the *overlap in information content* between two variables:

$$\mathrm{MI}(A;B) = H(A) - H(A|B). \tag{4.6}$$

We note that MI is symmetric in A and B, i.e., $\mathrm{MI}(A;B) = \mathrm{MI}(B;A)$. It is zero when A and B are statistically independent, indicating that observing A provides no additional information about B and vice versa [92]. A Normalized Mutual Information (NMI) has been introduced in [94] as:

$$\mathrm{NMI}(A;B) = \frac{\mathrm{MI}(A;B)}{H(A) + H(B)}, \tag{4.7}$$

which takes a value between 0 and 1. If there is no shared information content between A and B, then $\mathrm{NMI}(A;B) = \mathrm{MI}(A;B) = 0$. The more the overlap in information content of A and B, the closer the NMI approaches a value of 1.

The formulations in (4.6) and (4.7) can be extended to also measure the overlap in the information content among sets of variables. For instance, the NMI between random variable A and the pair of random variables B and C is obtained as:

$$\mathrm{NMI}(A;B,C) = \frac{\mathrm{MI}(A;B,C)}{H(A) + H(B,C)}, \tag{4.8}$$

where

$$\mathrm{MI}(A;B,C) = H(A) - H(A|B,C). \tag{4.9}$$

Note that $H(A|B,C)$ is the conditional entropy of A, given both B and C. Again, the value of $\mathrm{NMI}(A;B,C)$ is always between 0 and 1, where 0 implies no shared information content

between A and (B, C). The closer $\mathrm{NMI}(A; B, C)$ is to 1, the more information content is shared by A and (B, C).

4.3.2 Information Content of Features in Phasor Measurements

In order to apply the above concepts to the context of our study, we take two steps. First, we represent the event signatures, whether in the fundamental phasor measurements or the harmonic phasor measurements, based on *features*, which represent a summary statistic of time series measurements. Second, we discretize the extracted features from the first step.

With regards to feature extraction, we start from the existing literature in the analysis of event signatures in phasor measurements. Specifically, we focus on extracting the features from the following time-series on each of the three phases [83]:

$$V_i, I_i, \cos(\theta_i - \phi_i), \quad i = 1, \ldots, m. \tag{4.10}$$

Note that, for $i = 1$, i.e., for the fundamental phasors, the term $\cos(\theta_i - \phi_i)$ in (4.10) is the same as power factor. However, for any $i > 1$, i.e., for harmonic phasor measurements, the term $\cos(\theta_i - \phi_i)$ in (4.10) can too be viewed as a notion of power factor, but based on harmonic phasors. Importantly, it is common *not* to directly use the phase angles of voltage and current in the analysis of events. Instead, the cosine of their difference is used to eliminate the impact of the fluctuations in the frequency of the power system, see [11, p. 114].

Let $X(t)$ denote a time-series from the list in (4.10)Suppose $\bar{X}_{\mathrm{pre}}$ and $\bar{X}_{\mathrm{post}}$ denote the *average* of $X(t)$ *before* and *after* the event, respectively. Furthermore, let $X_{\min}$ and $X_{\max}$

denote the *minimum* value and the *maximum* value of $X(t)$ during the event. We define two *features* with respect to each $X(t)$:

$$S = \bar{X}_{\text{post}} - \bar{X}_{\text{pre}} \tag{4.11}$$

and

$$T = \begin{cases} X_{\max} - \bar{X}_{\text{pre}} & \text{if } |X_{\max} - \bar{X}_{\text{pre}}| \geq |X_{\min} - \bar{X}_{\text{pre}}| \\ X_{\min} - \bar{X}_{\text{pre}} & \text{otherwise,} \end{cases} \tag{4.12}$$

where S is the change in the *steady-state* conditions of the time-series, before and after the event; and T is the maximum change in the *transient* conditions of the time-series during the event, either as overshoot or as undershoot during the event.

Importantly, for each event, the above two features are extracted from not only the event signatures in the *fundamental* phasor data but also the event signatures in the *harmonic* phasor data. Accordingly, a total of $6m$ features are extracted from the phasor data in (4.10) on each phase for each event.

The discretization of the extracted features is done by dividing the range of each continuous-valued feature into a number of bins (equal to the square root of the number of data points). This choice balances the objectives that discretization effects remain negligible for NMI measurements and that the numerical NMI estimates are sufficiently accurate.

We can incorporate each pair of the extracted discretized features as random variables A and B to obtain NMI as in (4.7). For example, A can be the transient change in the event signature in the fundamental phasor measurements and B can be the transient change in the event signature in the harmonic phasor measurements of the third harmonic. Accordingly, we can investigate the information content of the extracted features in the real-world power system events in the dataset.

Table 4.1: Normalized MI Among Certain Pairs of Features

	V	I	$\cos(\theta - \phi)$
NMI(T1;T3)	0.1034	0.0445	0.0208
NMI(T1;T5)	0.0653	0.0389	0.0217
NMI(S1;S3)	0.0524	0.0417	0.0191
NMI(S1;S5)	0.1386	0.0544	0.0203

In this study, we estimate the joint probability functions as well as the marginal probability distribution functions by discretizing the extracted features into bins, and using bivariate or multivariate histogram bin counts depending on the number of features. The results are then normalized based on the number of events. Marginal distributions are obtained by summing the joint probabilities for the two features.

4.4 Case Studies Using Field Data

4.4.1 Analysis of Pairwise Information Content

Suppose the harmonic phasor measurements are limited to the third harmonic phasors, and the fifth harmonic phasors. The results are shown in Table 4.1. Each row provides the NMI between a feature from the fundamental phasor measurements and a comparable feature from the harmonic phasor measurements. These results are based on taking the average of the NMI across all the power system events in the dataset. The features are extracted by (4.11) and (4.12). For example, T1 is the transition change in the event signature based on the fundamental phasor data, and S3 is the steady-state change in the event signature based on the third harmonic phasor data.

All the NMI values in Table 4.1 are close to 0, highlighting that every feature for every harmonic phasor that is listed in this table carries distinct information. The

varying levels of NMI values in this table suggest that the information overlap between these features are different for different features and for different harmonics. A lower value for NMI means that the second feature provides more additional information to the first feature. For example, consider the lowest value of NMI in the column under V, which is NMI(S1,S3) = 0.0524. This means that by using the steady-state changes in the voltage magnitude of the third harmonic phasors, we can most significantly increase the information content of the features, compared to the case where we only use the steady-state changes in the voltage magnitude of the fundamental phasors.

4.4.2 Application in Optimal Selection of Harmonic Phasors to Maximize Information Content in Event Signatures

Recall from Section 5.2 that an H-PMU may provide harmonic phasor measurements only for a small and specific number of harmonics. One may ask: *if we can only measure a few harmonic phasors, which ones should we pick for the analysis of events?* Next, we seek to answer this question.

Specifically, we compare two scenarios, which contain an equal number of harmonic phasors within their feature sets. Without loss of generality, we assume that only the magnitudes of the voltage phasors are used in this case study. Scenario 1 exclusively employs odd harmonic phasors:

$$\mathbf{V}_1\angle\boldsymbol{\theta}_1,\ \mathbf{V}_3\angle\boldsymbol{\theta}_3,\ \mathbf{V}_5\angle\boldsymbol{\theta}_5,\ \mathbf{V}_7\angle\boldsymbol{\theta}_7,\ \mathbf{V}_9\angle\boldsymbol{\theta}_9. \tag{4.13}$$

Scenario 2 employs both odd and even harmonic phasors:

$$\mathbf{V}_1\angle\boldsymbol{\theta}_1,\ \mathbf{V}_2\angle\boldsymbol{\theta}_2,\ \mathbf{V}_3\angle\boldsymbol{\theta}_3,\ \mathbf{V}_4\angle\boldsymbol{\theta}_4,\ \mathbf{V}_5\angle\boldsymbol{\theta}_5. \tag{4.14}$$

Table 4.2: Normalized MI for Two Different Scenarios for Choosing a Fixed Number of Harmonic Phasors

Selection Scenario 1	NMI(T1; T3, T5, T7, T9)	0.2463
	NMI(S1; S3, S5, S7, S9)	0.2620
Selection Scenario 2	NMI(T1; T2, T3, T4, T5)	0.1334
	NMI(S1; S2, S3, S4, S5)	0.1383

The above two scenarios use the same number of phasors, i.e., five. The question is: *which scenario carries more information about the event?* We can answer this question by conducting a *multivariate* mutual information analysis corresponding to the formulation in (4.8), but based on five variables to account for the number of phasors in (4.13) and (4.14). The results are shown in Table 4.2. We observe that, whether with respect to the transient features or with respect to the steady-state features, Scenario 2 has a lower NMI than Scenario 1 on average:

$$\begin{aligned} &\text{NMI(T1; T2, T3, T4, T5)} < \text{NMI(T1; T3, T5, T7, T9)} \\ &\text{NMI(S1; S2, S3, S4, S5)} < \text{NMI(S1; S3, S5, S7, S9).} \end{aligned} \tag{4.15}$$

That means that the features in Scenario 2 have less information overlap with the features of the fundamental phasors than those in Scenario 1. Thus, the event signatures in Scenario 2 are expected to be more informative with respect to the characteristics of the events than the event signatures in Scenario 1. This approach can help with systematic and optimal selection of the harmonic phasors to maximize their information content.

We note that the above results are in contrast to the traditional analysis of harmonics in the field of power quality, where even harmonics are almost never considered due to the often symmetric nature of voltage waveforms in steady-state conditions. However,

when it comes to the analysis of power system events, the above results suggest that the use of even harmonics, as in Scenario 2, can be beneficial.

4.4.3 Application in Event Clustering

The additional information content of H-PMU measurements can improve the performance of event-based tasks in power systems. An example is in the field of event clustering and event classification, where we seek to identify the type or cause of an event based on its signatures in the measurements.

Fig. 4.2 depicts the use of harmonic phasor measurements in event clustering. The clusters are obtained by using K-means clustering for different choices of the feature space. Different subfigures demonstrate different harmonic phasor signature feature spaces, while sharing a *common color-coding*. The color coding is based on clustering of the events with respect to their S and T features as captured in Fig. 4.2(a) based on the fundamental phasor measurements. This representation provides a baseline scenario to assess how the events that may seemingly belong to the same cluster appear very differently based on their features in the higher harmonic spaces.

To see this, consider the feature spaces in Figs. 4.2(b) and (c), which are based on the features that are extracted from the third and the fifth harmonic phasor measurements, respectively. Note that the colors represent the *same clusters* that were identified in Fig. 4.2(a), based on the features from the *fundamental* phasor measurements.

The comparison of Figs. 4.2(a), (b), and (c) confirms that the clusters based on the features in the fundamental phasor measurements are *not* valid for the higher harmonic feature spaces. This discrepancy demonstrates that clustering based purely on fundamental

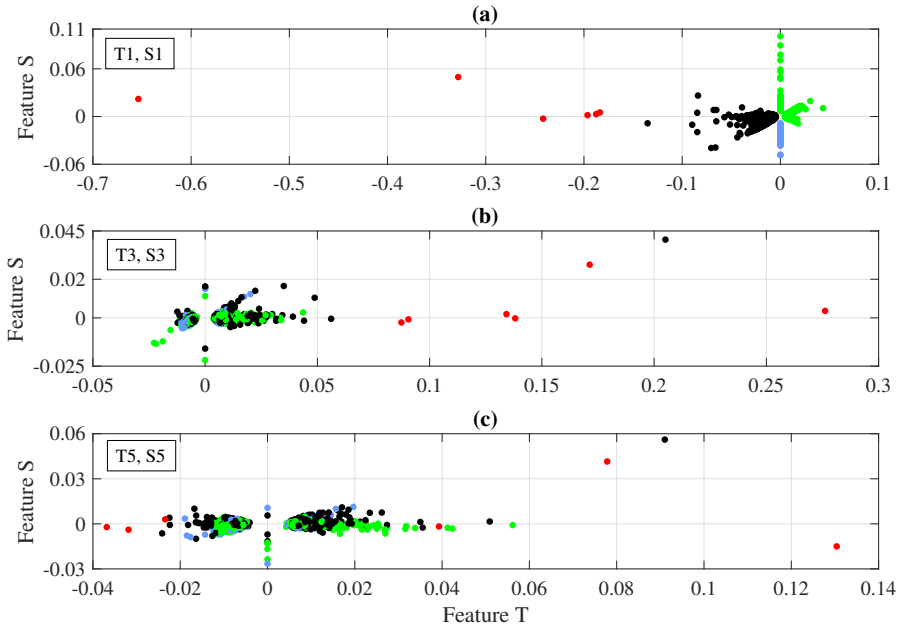

Figure 4.2: (a) Fundamental phasor signature feature space, (b) Third harmonic phasor signature feature space, (c) Fifth harmonic phasor signature feature space. In all subfigures, the color coding is based on clustering of the events with respect to their S and T features in the fundamental phasors.

phasors may not fully capture the characteristics that are hidden in the higher harmonic phasor features.

Since the event data in real-world power systems is predominantly *unlabeled*, we propose to use the silhouette value to assess the performance in event clustering, leveraging the various features derived in our analysis. Silhouette value indicates how well each object lies within its cluster. Specifically, it is a measure of how similar an object is to its own cluster (cohesion) compared to other clusters (separation) [95].

The silhouette value ranges between -1 and 1. A higher value indicates a better *clustering quality* of the power system events. Without loss of generality, we assume that

Table 4.3: Silhouette Values for 4 Clusters

Harmonic Phasor Features	I	V	$\cos(\theta - \phi)$
Fundamental	0.174	0.2151	0.2248
Fundamental and Third	0.2884	0.4526	0.3432
Fundamental and Third and Fifth	0.3547	0.677	0.5011

the number of clusters is fixed at four. That is, the target in each clustering task is to create four clusters based on certain features.

Table 4.3 shows the silhouette values obtained for different scenarios, i.e., 1) when we use only the features from the fundamental phasors, 2) when we use the features from the fundamental phasors and the third harmonic phasors, and finally, 3) when we use the features from the fundamental phasors, the third harmonic phasors, and the fifth harmonic phasors.

By comparing the results in Table 4.3 we can conclude that the silhouette values are highest in all variables when all features are included in the event clustering task. This outcome supports the premise that the inclusion of the features from the event signatures in the harmonic phasor measurements, particularly both the third and fifth harmonics, can significantly enhance the event clustering performance.

Chapter 5

Data-Driven Models for Sub-Cycle Dynamic Response of Inverter-Based Resources Using WMU Measurements

5.1 Introduction

With the increasing penetration of inverter-based resources, power systems are becoming more complex and more dynamic. Further, the recent incidents with the unexpected responses of IBRs to system-wide disturbances, such as in California, have underlined the need to monitor and characterize the dynamic behavior of IBRs at *high-resolution waveform levels*, such as within the short period of one AC cycle [96, 97].

However, the measurements from phasor measurement units that are commonly used in this field do *not* provide the type of data that is needed for this kind of analysis.

Instead, we need to use the measurements from waveform measurement units. WMUs are a new class of smart grid sensors that have emerged only recently [11, Section 4.6]. WMUs provide time stamped waveform measurements.

In this study, we use WMU data from a pilot project in California to address the above open problem. Specifically, we develop new *data-driven* methods to estimate the dynamic response of IBRs to system-wide sub-cycle disturbances.

To the best of our knowledge, this is the first study of its kind. In fact, as it is recently surveyed in [98], the existing methods in this field can be divided into two categories. First, there are methods that use the internal physics of the IBR [99, 100, 101]. Clearly, such methods require access to the internal physical systems for each IBR. Second, there are methods that are data-driven [102]. However, so far, the focus has been primarily on using data from PMUs. In this study we rather use data from WMUs.

5.2 Problem Statement

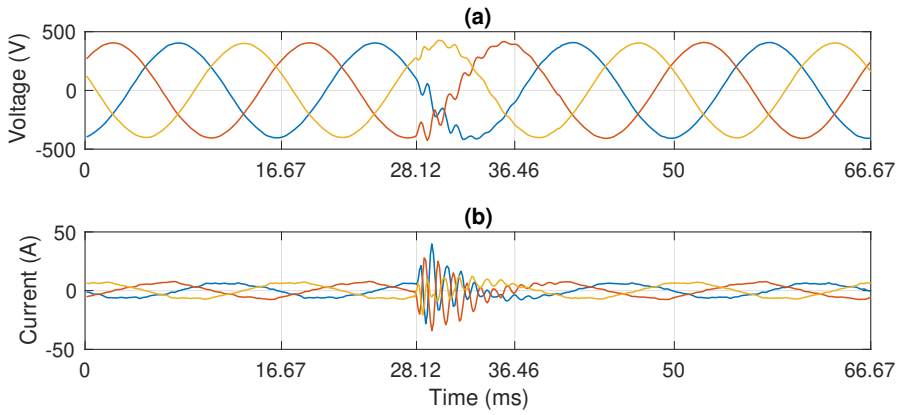

Figure 5.1: An IBR's response to a real-world system-wide sub-cycle disturbance: (a) the disturbance causes momentary distortions in voltage waveforms; (b) the dynamic response by the IBR is in form of momentary agitations in current.

Fig. 5.1 shows the *real-world* waveform measurements during a system-wide disturbance that is captured by a WMU at a three-phase PV unit. The disturbance causes a voltage event at the location of the PV inverter. This in turn, causes an agitation (response) in the PV inverter's current waveforms.

The impact of the *exact same disturbance* on another PV unit is shown in Fig. 5.2. The measurements in this figure are from another WMU. They are time-synchronized with the measurements at the first WMU. Thus, the measurements in Figs. 5.1 and 5.2 provide us with *synchro-waveform measurements*, to enable us compare the dynamic response of the two PV inverters (i.e., the two IBRs) to the same disturbance; see [103]. Importantly, the second IBR is located on a different feeder. Notice that, the response of the IBR in

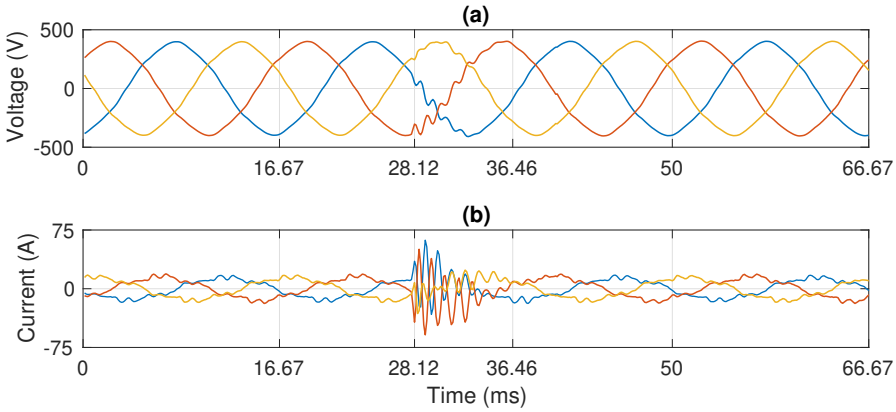

Figure 5.2: Another IBR's response to the exact same real-world system-wide sub-cycle disturbance: (a) the voltage distortion at the second IBR; (b) the dynamic response of the second IBR in form of momentary agitation in current.

Fig. 5.2(b) is different from the response of the IBR in Fig. 5.1(b). Whether in Fig. 5.1 or in Fig. 5.2, the disturbances as well as the responses of the IBRs are all very short, lasting only about half of a cycle.

5.2.1 IBR as a Dynamic System at Waveform Level

Based on the above examples, each IBR can be seen as a dynamic system that responds to the very fast and very short disturbances in the power system. Each IBR responds to the disturbances based on its own unique internal dynamics.

Accordingly, we can model the behavior of each IBR at *waveform level* as a dynamic system. Such system can be represented as an input-output box, as shown in Fig. 5.3. Here, the input signal is the disturbance in voltage waveform at the terminals of the IBR, and the output signal is the agitation in the IBR's current waveform in response to the disturbance.

Figure 5.3: The waveform-level input-output dynamic model of an IBR.

5.2.2 Waveform Representation in Differential Form

The disturbance in voltage waveforms as well as the IBR's dynamic response in the current waveforms can be best anlyzed once they are represented in *differential form*. Let time t_0 denote the moment when the disturbance starts. We can express the differential waveform corresponding to waveform $x(t)$ with respect to the event as follows [11, Section 4.2.5]:

$$\Delta x(t) = x(t) - x(t - T), \quad \forall\, t \geq t_0, \tag{5.1}$$

where $T = 1/60$ seconds is the waveform interval. Time t_0 can be obtained by using the existing methods in [11, Section 4.2]. Fig. 5.4 shows the differential waveforms corresponding to the disturbance in Fig. 5.1. Only Phase A is shown here. We can now clearly see the fast dynamic behavior of the IBR at this short interval; which is caused in response to the disturbance.

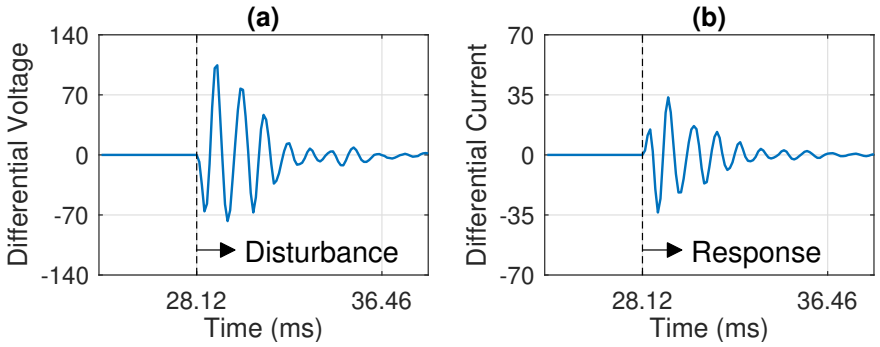

Figure 5.4: Differential waveforms for Phase A of the waveforms in Fig. 5.1.

5.2.3 Our Objective

For the rest of this study, our objective is to develop *data-driven* models to capture the dynamic response of the IBR, i.e., to predict the IBR's injected current in differential waveform in response to a disturbance in voltage in differential waveform.

5.3 Model Construction in Frequency Domain Using Modal Analysis and Library Development

Consider the differential voltage waveform (input signal) in Fig. 5.4(a) and the differential current waveform (output signal) in Fig. 5.4(b). We refer to them as $\Delta v(t)$ and $\Delta i(t)$. By applying the modal analysis, such as the Prony method [11, Section 2.6.3], we can express these two differential waveforms as:

$$\Delta v(t) = \sum_{m=1}^{M} A_m e^{\sigma_m t} \cos(\omega_m t + \phi_m), \tag{5.2}$$

$$\Delta i(t) = \sum_{m=1}^{M} B_m e^{\sigma_m t} \cos(\omega_m t + \psi_m), \tag{5.3}$$

where M denotes the number of dynamic modes. Each dynamic mode m is represented by angular frequency ω_m and damping factor σ_m. The differential voltage waveform at mode m is represented by magnitude A_m and phase angle ϕ_m. The differential current waveform at mode m is represented by magnitude B_m and phase angle ψ_m. Accordingly, at each mode m, we can define the equivalent admittance of the IBR at that particular mode as the following complex number:

$$\mathbf{H}_m = \frac{B_m \angle \psi_m}{A_m \angle \phi_m} = \frac{B_m}{A_m} \angle (\psi_m - \phi_m) \quad \text{at} \quad \omega_m + j\sigma_m. \tag{5.4}$$

5.3.1 Data-Driven Library Construction

Suppose the voltage and current waveforms are available from a WMU at an IBR during K disturbances. Let $\Delta v^1(t), \ldots, \Delta v^K(t)$ denote the differential voltage waveforms and $\Delta i^1(t), \ldots, \Delta i^K(t)$ denote the differential current waveforms during disturbances $k = 1, \ldots, K$. By applying the analysis in (5.2)-(5.4) to the above measurements, we can obtain:

$$\mathbf{H}_m^k \quad \text{at} \quad z_m^k = \omega_m^k + j\sigma_m^k, \qquad \begin{matrix} k = 1, \ldots, K, \\ m = 1, \ldots, M. \end{matrix} \tag{5.5}$$

Each model in (5.5) corresponds to *one* dynamic mode that is derived from the analysis of *one* disturbance; thus adding up to build a *library* of $K \times M$ models using modal analysis.

5.3.2 Data-Driven Model Selection

Let $\Delta v_{\text{test}}(t)$ denote the differential voltage waveform for the given disturbance. Let $\Delta i_{\text{test}}(t)$ denote the differential current waveform for the response of the IBR to this disturbance. Given $\Delta v_{\text{test}}(t)$, we seek to estimate $\Delta i_{\text{test}}(t)$ based on the model library in (5.5). We denote our estimate by $\hat{\Delta} i_{\text{test}}(t)$.

Let us denote the dynamic modes of the test input signal $\Delta v_{\text{test}}(t)$ by $z_{n,\text{test}} = \omega_{n,\text{test}} + j\sigma_{n,\text{test}}$, where $n = 1, \ldots, M$. For any such dynamic mode n, we define $k_n^\star$ and $m_n^\star$ as follows:

$$[\, k_n^\star, m_n^\star \,] = \arg\min_{k,m} \left| z_{n,\text{test}} - z_m^k \right|^2. \tag{5.6}$$

Here, we select one dynamic mode from the library in (5.5) that has the *minimum distance* from dynamic mode n of the test input signal.

We estimate the IBR's response to $\Delta v_{\text{test}}(t)$ as:

$$\hat{\Delta} i_{\text{test}}(t) = \sum_{n=1}^{M} C_n e^{\sigma_{n,\text{test}} t} \cos(\omega_{n,\text{test}} t + \varphi_n), \tag{5.7}$$

where

$$C_n = A_{n,\text{test}} \left| \mathbf{H}_{m_n^\star}^{k_n^\star} \right|, \quad \varphi_n = \phi_{n,\text{test}} + \angle \mathbf{H}_{m_n^\star}^{k_n^\star}. \tag{5.8}$$

Here, $A_{n,\text{test}}$ and $\phi_{n,\text{test}}$ are the magnitude and phase angle for modal representation of $\Delta v_{\text{test}}(t)$ at its dynamic mode $z_{n,\text{test}}$. We use the magnitude and phase angle of the proper equivalent admittance from the model library to obtain C_n and ϕ_n in (5.8), which we use in (5.7) to estimate the IBR's response, denoted by $\hat{\Delta} i_{\text{test}}(t)$. As for indices $k_n^\star$ and $m_n^\star$ that are used in (5.8), they are defined in (5.6) and are used in order to select the proper model among the equivalent admittances in the model library. Notice that matrix $\mathbf{H}$ is defined in (5.4). In order to select the proper choice of $\mathbf{H}$ from the library of models in (5.5), we use indices $m_n^\star$ and $k_n^\star$, which are defined in (5.6).

5.4 Model Construction in Time Domain Using Regression Analysis and Library Development

Again consider the differential waveforms in Fig. 5.4. In this section, we represent $\Delta v(t)$ as $\Delta v[1], \Delta v[2], \ldots, \Delta v[N]$, which is a discrete time-series, where N is the number of samples. Similarly, we represent $\Delta i(t)$ as $\Delta i[1], \Delta i[2], \ldots, \Delta i[N]$.

5.4.1 Data-Driven Library Construction

Next, we use two different time-domain models, with and without auto-regression, to build the data-driven model library:

Approach 1: Using FIR Models

The response of the IBR is constructed by a Finite Impulse Response (FIR) model:

$$\Delta i[\tau] = b_1 \Delta v[\tau] + b_2 \Delta v[\tau - 1] + \ldots + b_{n_b} \Delta v[\tau - n_b + 1]. \tag{5.9}$$

The above FIR model estimates each sample of the output signal as a weighted sum of the n_b most recent samples of the input signal. Here, n_b denotes the order of the model.

Approach 2: Using ARX Models

The IBR's response is constructed by an Auto-Regressive eXogenous (ARX) model:

$$\begin{aligned} \Delta i[\tau] = a_1 \Delta i[\tau - 1] + \cdots + a_{n_a} \Delta i[\tau - n_a] + b_1 v[\tau] \\ + b_2 \Delta v[\tau - 1] + ... + b_{n_b} \Delta v[\tau - n_b + 1]. \end{aligned} \tag{5.10}$$

This ARX model estimates each sample of the output signal as a weighted sum of the n_b most recent samples of the input signal and the n_a most recent samples of the output signal itself. Here, n_a and n_b denote the order of the model.

Given the K training data sets, we can use (5.9) or (5.10) to build a library of K FIR models or K ARX models. For each model, we need to estimate the corresponding unknowns as:

$$\boldsymbol{\theta}_{\text{FIR}} = [b_1, \cdots, b_{n_b}]^\top, \tag{5.11}$$

$$\boldsymbol{\theta}_{\text{ARX}} = [a_1, \cdots \ a_{n_a}, b_1, \cdots, b_{n_b}]^\top. \tag{5.12}$$

Vectors $\boldsymbol{\theta}_{\text{FIR}}$ and $\boldsymbol{\theta}_{\text{ARX}}$ can be obtained using methods such as Least Square (LS) optimization, e.g., [104, Section 3.2].

5.4.2 Model Selection

Similar to the analysis in Section 5.3.2, we need a method to select the proper model from the library. However, since we do not use modal analysis in Section 5.4, we select the model based on directly comparing the time series of the test input signal and the time series of the training input signals:

$$k^\star = \arg\min_k \sum_{\tau=1}^{N} \left| v^k[\tau] - v_{\text{test}}[\tau] \right|^2 . \tag{5.13}$$

Given $k^\star$, we can estimate $\Delta i_{\text{test}}(t)$ by using either the FIR model in (5.9) and (5.11) or the ARX model in (5.10) and (5.12).

5.5 Potential Applications

The analysis in this paper can be used in various potential applications. First, the models for the dynamic response of IBRs can be used for *diagnosis* purposes to enhance the life span of IBRs. This can be done by comparing the derived data-driven models with the nominal/reference models that are provided by the IBR manufacturers. Another option is to *regularly monitor* the dynamic behavior of each IBR over time. A major change can potentially indicate an *incipient failure* that may suggest the need for inspection or maintenance. Second, modeling the sub-cycle dynamic behavior of IBRs may also help with developing digital twins for different types of IBRs to predict how different IBRs may respond to various disturbances in power systems. This can ultimately help with identifying

the type and magnitude of disturbances that are likely to cause undesirable tripping of IBRs; see [96] for a related discussion. Third, the analysis in this paper can also be used to *compare* the dynamic response of a large group of IBRs in a given geographical region. Such analysis may also shed light on potential *ripple effects* in the power system that may follow a system-wide disturbance due to the agitations in power production or even momentary secession of IBRs.

5.6 Case Studies

In this section, we apply the proposed methods to the *real-world* waveform measurements that are obtained by a WMU at a 480 V / 100 kW PV unit, for six months. In total, 63 sub-cycle system-wide disturbances and the corresponding responses of the IBR were recorded in this period. Out of the 63 available disturbances, we used 42 disturbances for training the model, i.e., two third of the available disturbances in the data set is used for training. The remaining 21 disturbances are used for testing the accuracy of the model, i.e., one third of the available disturbances in the data set is used for testing. As a result, we evaluated the *out-of-sample* performance of the proposed models; because the samples that we used for performance evaluation had *no overlap* with the samples that we used to obtain (i.e., train) the models.

5.6.1 Comparison with Baseline Methods

As the baseline method to be compared with the design in Section 5.3, we consider a method that applies multi-signal modal analysis to all the 42 training data sets to develop

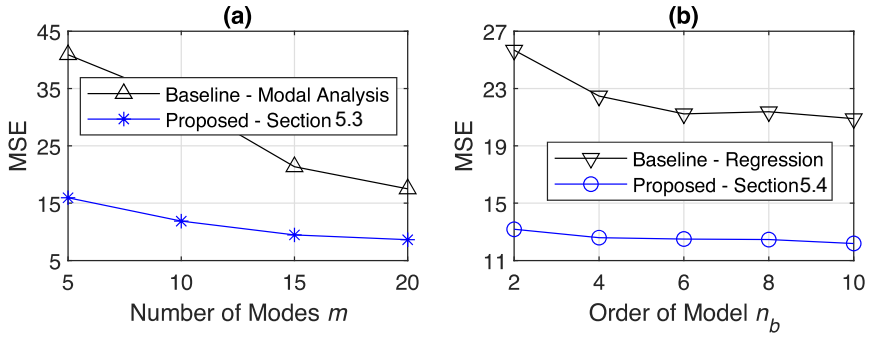

Figure 5.5: Performance comparison with the corresponding baseline methods: (a) for the method in Section 5.3; (b) for the method in Section 5.4.

a *single* model in frequency domain. That is, *unlike* our proposed method in Section 5.3, this baseline method does *not* involve the library construction in (5.5) and the model selection in (5.6). The results are shown in Fig. 5.5(a), in terms of the Mean Squared Error (MSE) for each method. As we can see, both methods improve as we increase the number of modes. However, the proposed method always performs much better than the baseline method.

As the baseline method for the design in Section 5.4, we consider a method that applies multi-signal regression to all the 42 training data sets to develop a *single* model in time domain. That is, *unlike* our proposed method in Section 5.4, this baseline method does *not* involve library construction and model selection. The results are shown in Fig. 5.5(b). In both cases, we use FIR models. As we can see, the proposed method always performs much better than the baseline method.

5.6.2 Analysis of Modal Distance

For the method in Section 5.3, it is insightful to examine the MSE as a function of the *modal distance* between each test input signal and the training input signals. For each $\Delta v_{\text{test}}(t)$, we obtain:

$$\text{Modal Distance:} \quad \Phi = \sqrt{\sum_{n=1}^{M} \left| z_{n,\text{test}} - z_{m_n^\star}^{k_n^\star} \right|^2}. \tag{5.14}$$

The results are shown in Fig. 5.6. A trend is evident. In general, a higher modal distance for a test input signal leads to a higher MSE in estimating its corresponding test output signal.

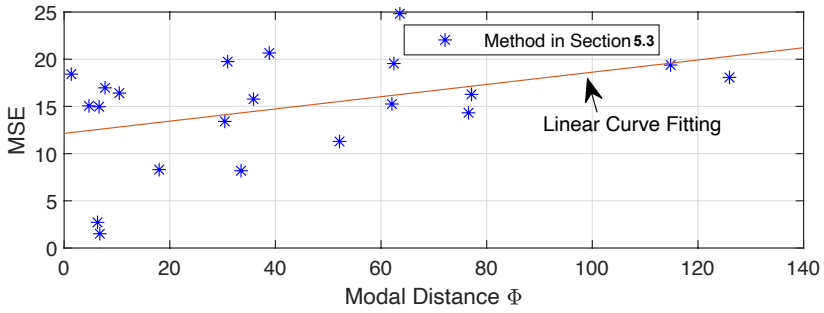

Figure 5.6: Plotting the individual MSE of each test case versus the modal distance between the test input signal and the training input signals. Parameter $M = 6$.

5.6.3 Using FIR vs. ARX Model

For the proposed method in Section 5.4, Table 5.1 compares the performance of using the FIR model versus the ARX model. The FIR model shows a *more stable* performance, i.e., its MSE consistently improves as we increase the order of the model. The

Table 5.1: MSE for Using FIR VS. ARX Models in Section 5.4

	$n_b = 2$	$n_b = 3$	$n_b = 4$	$n_b = 5$
FIR	13.1761	12.7091	12.5947	12.5859
ARX ($n_a = 1$)	12.4331	12.6453	12.4619	12.3848
ARX ($n_a = 2$)	12.5315	**12.3748**	12.4892	13.4232

ARX model rather needs proper tuning of its parameters. However, once such tuning is done, the ARX model can perform slightly better than the FIR model. In fact, the best result in Table 5.1, in bold, is achieved when we use the ARX model with $n_a = 2$ and $n_b = 3$.

Chapter 6

Conclusions and Future Work

6.1 Summary of Conclusions

The goal of this thesis was to enhance situational awareness in power distribution systems, particularly focusing on the challenges posed by limited harmonic-observability and the integration of renewable energy sources. By developing novel physics-aware harmonic state estimation methods and utilizing data-driven approaches, this work aims to provide power distribution system operators with advanced tools to monitor and analyze harmonic distortions and dynamic behaviors effectively.

In Chapter 2, a novel physics-aware sparse HSE formulation was developed for radial power distribution systems under low-observability conditions. This design extracts various individual and group sparsity patterns in harmonic nodal injection current phasors, harmonic line current phasors, and harmonic nodal voltage phasors with respect to the location of the harmonic source. The HSE problem is formulated as a constrained weighted Lasso optimization. Our analysis covers the challenging scenario where the location of

the harmonic source is unknown, and multiple case studies in OpenDSS confirmed the effectiveness of the proposed method.

In Chapter 3, a novel physics-aware mixed-integer quadratic programming formulation and corresponding innovative algorithm were proposed to solve the HSE problem in low-observable power distribution feeders. This method extracts the sparsity patterns of harmonic state variables in the presence of multiple harmonic sources with unknown numbers and locations. Using the superposition theorem, this methodology uniquely integrates the process of obtaining the number and locations of harmonic sources with harmonic state estimation. The effectiveness of the proposed method was verified through various case studies and compared with existing methods.

In Chapter 4, new data-driven methods were developed and tested to model the dynamic behavior of inverter-based resources when responding to sub-cycle waveform disturbances. Experimental results confirmed the high performance of the methods compared to baselines, providing valuable insights to utilities and independent system operators for enhancing situational awareness and improving power system stability and reliability. Modeling the sub-cycle dynamic behavior of IBRs can help identify disturbances that can cause significant agitation or momentary cessation in power production, as well as potential ripple effects in the power system.

In Chapter 5, we explored the event signatures in harmonic phasor measurements recorded by H-PMUs to uncover new information about power system events not captured by fundamental phasor measurements from conventional PMUs. By applying techniques from information theory to real-world phasor measurements, we demonstrated that har-

monic phasors provide significant independent information content. This information is valuable for optimizing the selection of harmonic phasor orders for event analysis and enhancing the performance of event clustering in power system situational awareness. Incorporating harmonic features significantly improved event clustering performance, as evidenced by improved silhouette values. Future research can further explore the applications of this new direction in power system monitoring.

Overall, this thesis presents comprehensive methodologies for enhancing situational awareness in power distribution systems through advanced HSE techniques and data-driven dynamic response modeling, contributing significantly to the field of power system monitoring.

6.2 Future Work

While this thesis has made significant contributions to enhancing situational awareness in power distribution systems, there remain several avenues for future research to further advance this field.

The proposed methods in Chapters 2 and 3 took advantage of the radial topology of the power distribution system [57, 85]. Future research could examine cases where the network topology is not radial, adding complexity and requiring new approaches to HSE.

Further research could investigate the integration of the developed HSE methods with other power system applications, such as fault detection and localization, asset management, and predictive maintenance. This would provide a holistic approach to power system monitoring and control.

For the information-theoretic approaches in Chapter 4, we examined the information content of the harmonic phasors [105]. Future research could extend this to include wideband phasors, such as inter-harmonics, analyzing their information content and potential benefits for power system monitoring and situational awareness.

Lastly, in Chapter 5, the proposed method used modal analysis and regression models to estimate the IBRs' response to transient events [106]. Future work could employ machine learning methods, such as deep learning, to enhance the accuracy of these models. Additionally, future research could extend the analysis to different types of events, including voltage sags, frequency deviations, and other power quality disturbances. Methods could also be proposed to reuse or adjust a model from one IBR to capture the response of another IBR based on the analysis of time-synchronized waveform measurements at both IBRs.

Appendices

Appendix A

In this Appendix, we explain how to construct matrices $\mathbf{H}(h)$ and $\mathbf{G}(h)$ in order to formulate the equation in (3.5).

The measurement matrix $\mathbf{H}(h)$ contains two types of rows. The first type of rows in matrix $\mathbf{H}(h)$ is associated with harmonic voltage phasor measurements. The following relationship holds between the harmonic nodal injection current phasors and the harmonic voltage phasor measurements:

$$\mathbf{V}^m(h) = \mathbf{U}_V^m \mathbf{Y}^{-1}(h)\, \mathbf{I}_N(h), \tag{7.1}$$

where $\mathbf{U}_V^m \in \mathbb{R}^{|\mathcal{N}|\times|\mathcal{N}|}$ is a diagonal matrix,such that its diagonal entry in row i is 1 if the associated bus i is equipped with measurement, and otherwise it is zero. Also,

$\mathbf{Y}(h)$ is the admittance matrix for harmonic order h. In addition to (7.1), the harmonic voltage phasor measurements can be mapped also to their associated entries in the vector of harmonic voltage phasors through an identity mapping:

$$\mathbf{V}^m(h) = \mathbf{U}_V^m \, \mathbf{V}(h), \tag{7.2}$$

The second type of rows in matrix $\mathbf{H}(h)$ is associated with the harmonic line current measurements. The harmonic line current measurements are mapped to the vector of harmonic nodal voltage phasors as follows:

$$\mathbf{I}_L^m(h) = \mathbf{U}_I^m \mathbf{Y}_{\text{prim}}(h) \, \mathbf{V}(h), \tag{7.3}$$

where $\mathbf{U}_I^m \in \mathbb{R}^{|\mathcal{L}| \times |\mathcal{L}|}$ is a diagonal matrix, such that its diagonal entry in row i is 1 if the associated line segment i is equipped with measurement, and otherwise it is zero. Also, $\mathbf{Y}_{\text{prim}}(h)$ is the primitive admittance matrix [42], which includes the line admittances only for the line segments whose harmonic current phasors are measured. Harmonic line current phasor measurements can also be related to the vector of the harmonic line current phasors through an identity mapping:

$$\mathbf{I}_L^m(h) = \mathbf{U}_I^m \, \mathbf{I}_L(h). \tag{7.4}$$

As for matrix $\mathbf{G}(h)$, it includes similar equations to (35). But for the line segments that are *not* equipped with H-PMUs, we use an equation that captures the relationship between the harmonic nodal voltage and the harmonic line currents:

$$\mathbf{0} = (\mathbf{I} - \mathbf{U}_I^m)(\mathbf{Y}_{\text{prim}}(h) \, \mathbf{V}(h) - \mathbf{I}_L(h)), \tag{7.5}$$

where $\mathbf{I} \in \mathbb{R}^{|\mathcal{L}|\times|\mathcal{L}|}$ is an identity matrix. The equations in (7.5) create more coupling among the state variables, which finally appears in (3.5) as:

$$\mathbf{0} = \mathbf{G}(h)\mathbf{X}(h). \tag{7.6}$$

It is worth mentioning that, for a network with low observability, it is crucial to use the augmented formulation in (3.5) in order to at least *include* the *unobservable* harmonic variables in the equations of the *HSE problem* formulation through the use of matrix $\mathbf{G}(h)$. Otherwise, there is no other place to include the unobservable harmonic variables in the formulation of the problem; which would *not* allow estimating them.

Appendix B

In this Appendix, we explain the key characteristics of the *substation connector path* that was mentioned in Section 3.3.1. In particular, we explain why the harmonic current *almost entirely* flows through the substation, i.e., through the substation connector path, which is marked in red in Fig. 3.1. The steps to explain this concept are shown in Fig. 7.1(a).

First, consider the network model in Fig. 7.1(a). Here, we have replaced the laterals with their equivalent impedance. In particular, we have replaced the lateral that contains buses 19 to 22 with impedance Z_{19-22}; the lateral that contains buses 23 to 25 with impedance Z_{23-25}; and the lateral that contains buses 26 to 33 with impedance Z_{26-33}. Furthermore, we replaced the part of the main feeder that is on the *right hand side* of the harmonic source at bus 13, i.e., the part that includes buses 14 to 18, with impedance Z_{14-18}. As for Z_{Thevein}, it denotes the impedance in the Thevenin equivalent of the substation that is seen by the distribution feeder.

In Fig. 7.1(a), since Z_{Thevein} and Z_{19-22} are in parallel; and because, in practice, the impedance of the power network as seen at the substation is much smaller than the impedance of any lateral [107], i.e., Z_{Thevenin} is much smaller than Z_{19-22}, we can conclude that no harmonic current will go through Z_{19-22}. Instead, almost the entire harmonic current will go through the substation. Therefore, we can eliminate the lateral and reduce the network model to Fig.7.1(b).

Similarly, in Fig.7.1(b), since Z_{Thevenin} and Z_{23-25} are in parallel, and Z_{Thevenin} is much smaller than Z_{23-25}, we can conclude that no harmonic current will go through

Z_{23-25}. Note that, with a slight abuse of notation, Z_{Thevenin} in Fig. 7.1(b) is redefined as the impedance of the Thevenin equivalent of the *combination* of the substation and bus 2. We can eliminate the lateral and reduce the network model to Fig.7.1(c).

Similarly, in Fig. 7.1(c), since Z_{Thevenin} and Z_{26-33} are in parallel, and Z_{Thevenin} is much smaller than Z_{26-33}, we can conclude that no harmonic current will go through Z_{26-33}. Therefore, we can eliminate the lateral and reduce the network model to Fig. 7.1(d). So far, all the laterals are eliminated.

Finally, in Fig. 7.1(d), since Z_{Thevenin} and Z_{14-18} are in parallel, and Z_{Thevenin} is much smaller than Z_{14-18}, we can conclude that no harmonic current will go through Z_{14-18}. Therefore, almost the entire harmonic current flows from the harmonic source to the substation through the substation connector path, as it is marked on the figure.

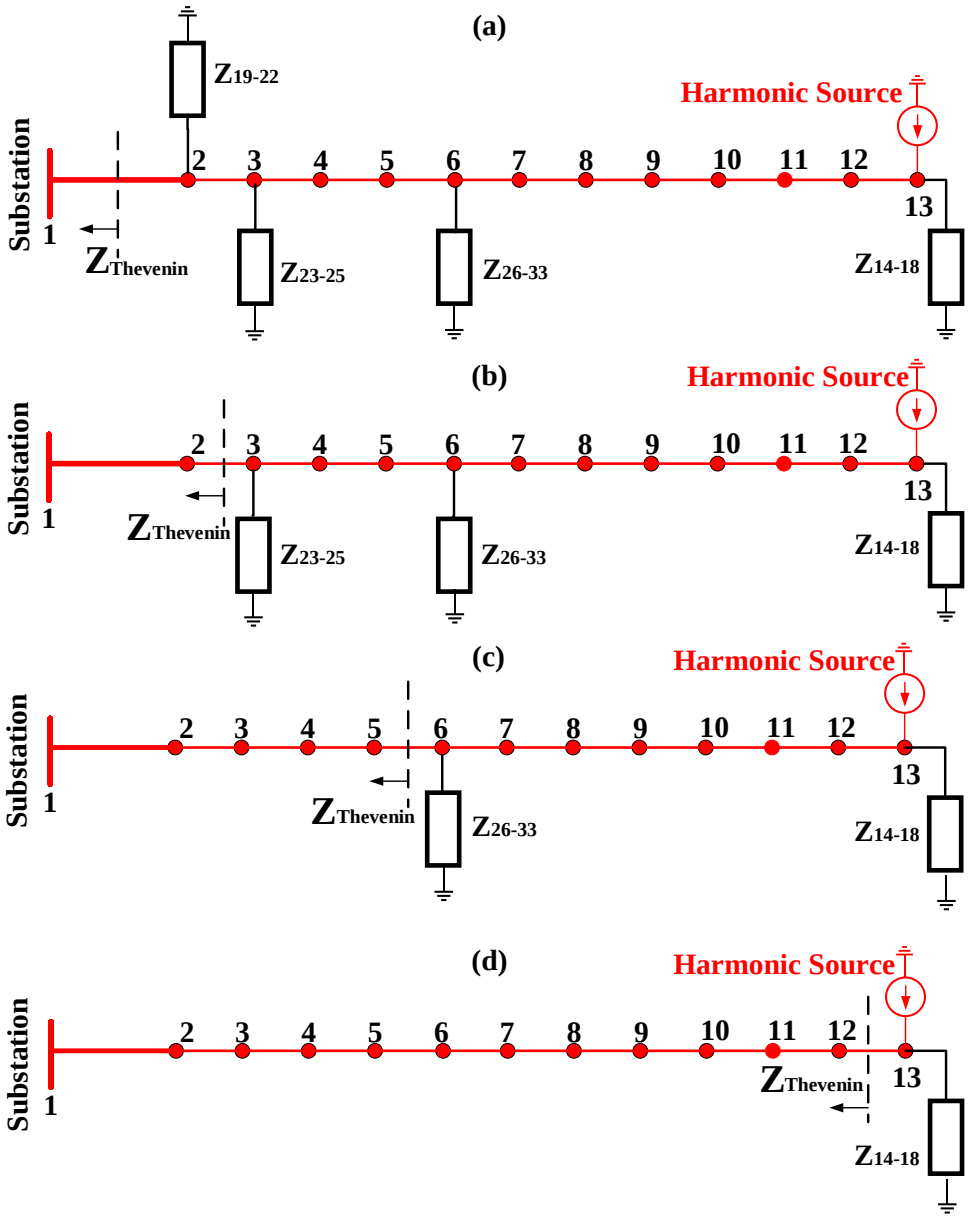

Figure 7.1: The illustration of the explanations in the Appendix about the characteristics of the substation connector path: (a) replacing the laterals in Fig. 1 with their equivalent impedances; (b) eliminating the first lateral; (c) eliminating the second lateral; (d) eliminating the third lateral.

Appendix C

In this appendix, we explain why it is necessary to consider *both* $\mathbf{V}(h)$ and $\mathbf{I}_L(h)$ as state variables in our HSE problem in Chapters 2 and 3.

Consider the small network in Fig.7.2. The network has five buses. One H-PMU is installed at bus 1 and another H-PMU is installed at bus 5. The H-PMU at bus 1 measures the harmonic nodal voltage phasor at bus 1 and the harmonic line current phasor at line L_1. The H-PMU at bus 5 measures the harmonic nodal voltage phasor at bus 5 and the harmonic line current phasor at line L_4. Accordingly, the vector of harmonic phasor measurements at harmonic order h is:

$$\mathbf{Z}(h) = [V_1(h)^m \;\; V_5(h)^m \;\; I_{L_1}(h)^m \;\; I_{L_4}(h)^m]^\top, \tag{7.7}$$

where superscript m indicates a measurement to distinguish the measurements from the state variables. To see the importance of including the line current phasors in the vector of state variables, let us hypothetically assume that we consider *only* the harmonic nodal voltage phasors as state variables:

$$\mathbf{X}(h) = [V_1(h)\; V_2(h)\; V_3(h)\; V_4(h)\; V_5(h)]^\top. \tag{7.8}$$

From (3.3), we would have the following system of equations:

$$\begin{bmatrix} V_1^m(h) \\ V_5^m(h) \\ I_{L_1}(h)^m \\ I_{L_4}(h)^m \end{bmatrix} = \Big[\mathbf{S}\Big] \begin{bmatrix} V_1(h) \\ V_2(h) \\ V_3(h) \\ V_4(h) \\ V_5(h) \end{bmatrix}. \tag{7.9}$$

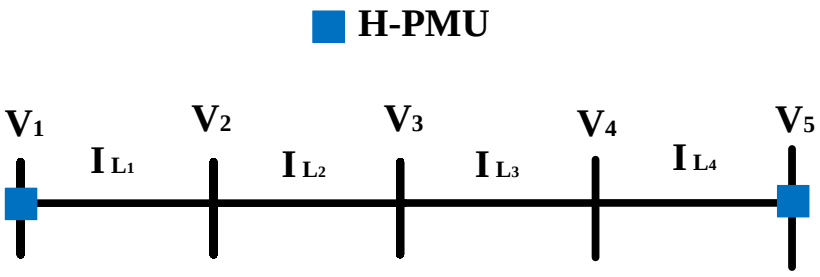

Figure 7.2: An illustrative example for the discussion in Appendix C: A small distribution feeder with 5 buses and 4 lines. Only two buses have H-PMUs.

where

$$\left[\mathbf{S}\right] = \begin{bmatrix} 1 & 0 & 0 & 0 & 0 \\ 0 & 0 & 0 & 0 & 1 \\ y_{L_1}(h) & -y_{L_1}(h) & 0 & 0 & 0 \\ 0 & 0 & 0 & y_{L_4}(h) & -y_{L_4}(h) \end{bmatrix}.$$

The above system of equations does not involve $V_3(h)$; because the associated coefficients are zero in all the rows. Thus, it is *impossible* to estimate $V_3(h)$ from the above equations; because $V_3(h)$ is simply *not* part of the equations.

If we do include the harmonic line current phasors in state variables, which is what we do in this paper, we would have:

$$\mathbf{X}(h) = [V_1(h) \ ... \ V_5(h) \ I_{L_1}(h) \ ... \ I_{L_4}(h)]^\top. \tag{7.10}$$

From (3.5), we would have the following system of equations:

$$\begin{bmatrix} V_1^m(h) \\ V_5^m(h) \\ I_{L_1}(h)^m \\ I_{L_4}(h)^m \\ 0 \\ 0 \end{bmatrix} = \Big[\mathbf{R}\Big] \begin{bmatrix} V_1(h) \\ V_2(h) \\ V_3(h) \\ V_4(h) \\ V_5(h) \\ I_{L_1}(h) \\ I_{L_2}(h) \\ I_{L_3}(h) \\ I_{L_4}(h) \end{bmatrix}, \tag{7.11}$$

where

$$\Big[\mathbf{R}\Big] = \begin{bmatrix} 1 & 0 & 0 & 0 & 0 & 0 & 0 & 0 & 0 \\ 0 & 0 & 0 & 0 & 1 & 0 & 0 & 0 & 0 \\ \frac{y_{L_1}(h)}{2} & -\frac{y_{L_1}(h)}{2} & 0 & 0 & 0 & \frac{1}{2} & 0 & 0 & 0 \\ 0 & 0 & 0 & \frac{y_{L_4}(h)}{2} & -\frac{y_{L_4}(h)}{2} & 0 & 0 & 0 & \frac{1}{2} \\ 0 & -y_{L_2}(h) & y_{L_2}(h) & 0 & 0 & 0 & -1 & 0 & 0 \\ 0 & 0 & -y_{L_3}(h) & y_{L_3}(h) & 0 & 0 & 0 & -1 & 0 \end{bmatrix}.$$

The last two rows in (7.11) are corresponding to matrix $\mathbf{G}(h)$ that we defined in Section 3.2.2. Unlike in (7.9), the system of equations in (7.11) involves *all* the state variables. This is a *necessary* condition to estimate all the state variables in the system. This is why we have included the harmonic line current phasors in the vector of the state variables in this study.

Bibliography

[1] J. D. Glover, T. J. Overbye, and M. S. Sarma, *Power system analysis and design*. Cengage Learning, 2017.

[2] M. H. Bollen, *Understanding Power Quality Problems*. Wiley-IEEE Press, 2000.

[3] T. L. Vu and K. Turitsyn, "A framework for robust assessment of power grid stability and resiliency," *IEEE Trans. on Automatic Control*, vol. 62, no. 3, pp. 1165–1177, 2017.

[4] S. Impram, S. V. Nese, and B. Oral, "Challenges of renewable energy penetration on power system flexibility: A survey," *Energy Strategy Reviews*, vol. 31, no. 100539, 2020.

[5] V. Prakash, P. Kushwaha, K. Chand Sharma, and R. Bhakar, "Frequency response support assessment from uncertain wind generation," *International Journal of Electrical Power Energy Systems*, vol. 134, no. 107465, 2022.

[6] F. Ahmed, D. Al Kez, S. McLoone, R. James Best, C. Cameron, and A. Foley, "Dynamic grid stability in low carbon power systems with minimum inertia," *Renewable Energy*, vol. 210, 2023.

[7] A. Ahmadian, B. Mohammadi-Ivatloo, and A. Elkamel, "A review on plug-in electric vehicles: Introduction, current status, and load modeling techniques," *Journal of Modern Power Systems and Clean Energy*, vol. 8, no. 3, 2020.

[8] A. M. Hariri, M. A. Hejazi, and H. Hashemi-Dezaki, "Investigation of impacts of plug-in hybrid electric vehicles' stochastic characteristics modeling on smart grid reliability under different charging scenarios," *Journal of Cleaner Production*, vol. 287, 2021.

[9] D. A. Z. Vazquez, F. Qiu, N. Fan, and K. Sharp, "Wildfire mitigation plans in power systems: A literature review," *IEEE Transactions on Power Systems*, vol. 37, no. 5, 2022.

[10] National Interagency Fire Center (NIFC), *Fire info*. 2020, [Online] https://www.mathworks.com/help/signal/ref/resample.html.

[11] H. Mohsenian-Rad, *Smart Grid Sensors: Principles and Applications*. Cambridge University Press, UK, 2021.

[12] TIB, NCS, "Supervisory Control and Data Acquisition (SCADA) Systems," National Communications System, TIB, Tech. Rep., 2004.

[13] W. R. Cassel, "Distribution management systems: functions and payback," *IEEE Trans. on Power Systems*, vol. 8, no. 3, pp. 796–801, 1993.

[14] H. Mohsenian-Rad, E. Stewart, and E. Cortez, "Distribution synchrophasors: pairing big data with analytics to create actionable information," *IEEE Power Energy Magazine*, vol. 16, no. 3, pp. 26–34, 2018.

[15] A. Carta, N. Locci, and C. Muscas, "A PMU for the measurement of synchronized harmonic phasors in three-piece distribution networks," *IEEE Trans. on Instrumentation and Measurement*, vol. 58, no. 10, pp. 3723–3730, Oct 2009.

[16] L. Chen, W. Zhao, F. Wang, and S. Huang, "Harmonic phasor estimator for P class phasor measurement units," *IEEE Trans. on Instrumentation and Measurement*, vol. 58, no. 10, pp. 1–10, May 2019.

[17] B. Zeng, Z. Teng, Y. Cai, S. Guo, and B. Qing, "Harmonic phasor analysis based on improved FFT algorithm," *IEEE Trans. on Smart Grid*, vol. 2, no. 1, pp. 51–59, Mar 2011.

[18] P. Rodríguez-Pajaró, A. Hernández, and J. V. Milanović, "Estimation of harmonics in partly monitored residential distribution networks with unknown parameters and topology," *IEEE Trans. on Smart Grid, doi: 10.1109/TSG.2022.3155976*, pp. 1–14, Mar 2022.

[19] L. Chen, M. Farajollahi, M. Ghamkhari, W. Zhao, S. Huang, and H. Mohsenian-Rad, "Switch status identification in distribution networks using harmonic synchrophasor measurements," *IEEE Trans. on Smart Grids*, vol. 12, no. 3, pp. 2413–2424, May 2021.

[20] M. Izadi and H. Mohsenian-Rad, "Characterizing synchronized lissajous curves to scrutinize power distribution synchro-waveform measurements," *IEEE Trans. on Power Systems*, vol. 36, no. 5, pp. 4880–4883, 2021.

[21] S. Bhela, V. Kekatos, and S. Veeramachaneni, "Enhancing observability in distribution grids using smart meter data," *IEEE Trans. on Smart Grid*, vol. 9, no. 6, p. 5953—5961, 2018.

[22] F. Ahmad, A. Rasool, E. Ozsoy, R. Sekar, A. Sabanovic, and M. Elita¸s, "Distribution system state estimation-a step towards smart grid," *Renewable and Sustainable Energy Reviews*, vol. 81, p. 2659—2671, 2018.

[23] I. T´aczi, B. Sinkovics, I. Vokony, and B. Hartmann, "The challenges of low voltage distribution system state estimation — an application oriented review," *Energies*, vol. 14, no. 17, p. 5363, 2021.

[24] W. Zhou, O. Ardakanian, H. Zhang, and Y. Yuan, "Bayesian learning-based harmonic state estimation in distribution systems with smart meter and DPMU data," *IEEE Trans. on Smart Grid*, vol. 11, no. 1, pp. 832–845, Jan 2020.

[25] X. Ji, Z. Yin, Y. Zhang, M. Wang, X. Zhang, C. Zhang, and D. Wang, "Real-time robust forecasting-aided state estimation of power system based on data-driven models," *Int. J. Electr. Power Energy Syst*, vol. 125, p. 106412, 2021.

[26] T. Ochi, D. Yamashita, K. Koyanagi, and R. Yokoyama, "The development and the application of fast decoupled load flow method for distribution systems with high r/x ratios lines," in *Proc. IEEE PES Innovative Smart Grid Technologies Conference (ISGT)*, 2013.

[27] F. Xu, C. Wang, K. Gue, Q. Shu, Z. Ma, and H. Zheng, "Harmonic sources' location and emission estimation in underdetermined measurement system," *IEEE Trans. on Instrumentation and Measurement, doi: 10.1109/TIM.2021.3077658*, vol. 70, May 2021.

[28] G. D'Antona, "Power system static-state estimation with uncertain network parameters as input data," *IEEE Transactions on Instrumentation and Measurement*, vol. 65, no. 11, p. 2485—2494, 2016.

[29] J. Qi, A. Taha, and J. Wang, "Comparing kalman filters and observers for power system dynamic state estimation with model uncertainty and malicious cyber attacks," *IEEE Access*, vol. 6, p. 77155—77168, 2018.

[30] Y. Wang, W. Xu, J. Yong, and K. L. Chen, "Estimating harmonic impact of individual loads using harmonic phasor data," *International Transactions on Electrical Energy Systems*, vol. 27, no. 10, p. e2384, 2017.

[31] D. Granados-Lieberman, "lobal harmonic parameters for estimation of power quality indices: An approach for pmus," *Energies*, vol. 13, no. 9, p. 2337, 2020.

[32] V. E. Wagner, J. C. Balda, D. C. Griffith, A. Mceachern, T. M. Barnes, D. P. Hartmann, D. J. Phileggi, A. E. Emannuel, W. F. Horton, W. E. Reid, and R. J. Ferraro, "Effects of harmonics on equipment," *IEEE Trans. Power Del.*, vol. 8, no. 2, pp. 672–680, Apr 1993.

[33] I. Molina-Moreno, A. Medina, R. Cisneros-Magaña, O. Anaya-Lara, and J. A. Salazar-Torres, "Enhanced harmonic state estimation in unbalanced three-phase electrical grids based on the kalman filter and physical scale-down implementation," *ELSEVIER*, vol. 123, Dec 2020.

[34] R. Cisneros-Magaña, A. Medina, V. Dinavahi, and A. Ramos-Paz, "Time-domain power quality state estimation based on kalman filter using parallel computing on graphics processing units," *IEEE Access*, vol. 6, pp. 21 152–21 163, Apr 2018.

[35] I. Molina-Moreno, A. Medina, R. Cisneros-Magaña, and O. Anaya-Lara, "Time domain harmonic state estimation in unbalanced power networks based on optimal number of meters and the principle of half-wave symmetry," *IET Generation, Transmission Distribution*, vol. 11, no. 15, pp. 3871–3880, Jun 2017.

[36] A. Medina and R. Cisneros-Magaña, "Time-domain harmonic state estimation based on the kalman filter poincare map and extrapolation to the limit cycle," *IET Generation, Transmission Distribution*, vol. 6, no. 12, pp. 1209–1217, Dec 2012.

[37] H. Liao, "Power system harmonic state estimation and observability analysis via sparsity maximization," *IEEE Trans. on Power Systems*, vol. 22, no. 1, pp. 15–23, Feb 2007.

[38] C. F. M. Almeida and N. Kagan, "Harmonic state estimation through optimal monitoring systems," *IEEE Trans. on Smart Grid*, vol. 4, no. 1, pp. 467–478, Mar 2013.

[39] D. Bhujel, N. Watson, and T. Jalal, "Application of harmonic state estimation to a distribution system," in *IEEE PowerTech*, Manchester, UK, Jul 2017.

[40] I. D. Melo, J. L. R. Pereira, A. M. Variz, and P. A. N. Garcia, "Harmonic state estimation for distribution networks using phasor measurement units," *Electric Power Sys. Research*, vol. 147, pp. 133–144, Jun 2017.

[41] D. Carta, C. Muscas, P. Pegoraro, and S. Sulis, "Identification and estimation of harmonic sources based on compressive sensing," *IEEE Trans. on Instrumentation & Measurement*, vol. 68, pp. 95–104, 2019.

[42] N. V. Ramana, *Power System Analysis*. Pearson, 2010.

[43] E. Michael, *Sparse and Redundant Representations: From Theory to Applications in Signal and Image Processing*. Springer, 2010.

[44] M. Farajollahi, A. Shahsavari, and H. Mohsenian-Rad, "Location identification of high impedance faults using synchronized harmonic phasors," in *IEEE PES ISGT, Arlington, VA,*, Apr 2017.

[45] L. Chen, M. Farajollahi, M. Ghamkhari, W. Zhao, S. Huang, and H. Mohsenian-Rad, "Switch status identification in distribution networks using harmonic synchrophasor measurements," *IEEE Trans. on Smart Grids*, vol. 12, no. 3, pp. 2413–2424, 2021.

[46] A. Akrami, S.Asif, and H. Mohsenian-Rad, "Sparse tracking state estimation for low-observable power distribution systems using D-PMUs," *IEEE Trans. on Power Systems*, vol. 37, no. 1, pp. 551–564, Jan 2022.

[47] J. A. Tropp, "Just relax: Convex programming methods for identifying sparse signals in noise," *IEEE Trans. on Information Theory*, vol. 52, no. 3, pp. 1030–1051, 2006.

[48] M. Grant and S. Boyd, "Cvx: Matlab software for disciplined convex programming, version 2.2," http://cvxr.com/cvx/, 2020, accessed: Jan 2020.

[49] M. E. Baran and F. F. Wu, "Network reconfiguration in distribution systems for loss reduction and load balancing," *IEEE Trans. on Power Delivery*, vol. 4, no. 2, pp. 1401–1407, Apr 1994.

[50] R. Dugan, *Reference Guide: OpenDSS*. EPRI, July, 2010.

[51] IEEE Standard, "IEEE recommended practices and requirements for harmonic control in electrical power systems," *IEEE Std 519-1992*, pp. 1–112, Apr 1993.

[52] J. Breda, J. Vieira, and M. Oleskovicz, "Three-phase harmonic state estimation for distribution systems by using the SVD technique," in *Power and Energy Society General Meeting (PESGM)*, Jul 2016.

[53] A. Arefi, M. Haghifam, and S. Fathi, "Distribution harmonic state estimation based on a modified pso considering parameters uncertainty," in *IEEE Trondheim PowerTech*, Sep 2011.

[54] T. Zang, Y. Wang, H. Sun, and Z. He, "Variable parameter kalman filter based dynamic harmonic state estimation for power systems with wind energy integration," in *Proc. of the IEEE Conference on Energy Internet and Energy System Integration*, Nov 2017.

[55] N. R. Watson, "Power quality state estimation," *European Trans. on Electrical Power*, vol. 20, no. 1, pp. 19–33, 2010.

[56] M. Haghifam and S. Fathi, "Distribution harmonic state estimation based on a hybrid PSO and SA algorithm considering parameters uncertainty," in *IEEE PES General Meeting (PESGM)*, Norway, Jul 2011.

[57] F. Ahmadi Gorjayi and H. Mohsenian-Rad, "Physics-aware sparse harmonic state estimation in power distribution systems," in *Proc. of the IEEE PES Conference on Innovative Smart Grid Technologies (ISGT), New Orleans, LA,*, Apr 2022.

[58] G. D'Antona, C. Muscas, and S. Sulis, "Localization of nonlinear loads in electric systems through harmonic source estimation," *IEEE Trans. on Instrumentation and Measurement*, vol. 60, no. 10, pp. 3423–3430, Oct 2011.

[59] R. Fernandes, M. Oleskovicz, and I. da Silva, "Harmonic source location and identification in radial distribution feeders: An approach based on particle swarm optimization algorithm," *IEEE Trans. on Industrial Informatics*, vol. 18, no. 5, pp. 3171–3179, May 2021.

[60] X. Chen, W. Feng, C. Shuyu, S. Chew, and K. Tseng, "PMU placement for measurement redundancy distribution considering zero injection bus and contingencies," *IEEE Systems Journal*, vol. 14, no. 4, pp. 5396–5406, May 2020.

[61] X. Zhu, M. Wen, V. Li, and K. Leung, "Optimal PMU-communication link placement for smart grid wide-area measurement systems," *IEEE Trans. on Smart Grid*, vol. 10, no. 4, pp. 4446–4456, Jul 2018.

[62] Z. Zhihua, Z. Qu, and J. Yang, "Optimal harmonic measuring device placement in distribution networks in consideration of topology changes," *IEEE Access*, vol. 8, pp. 85 339–85 347, May 2020.

[63] W. Li, D. Deka, M. Chertkov, and M. Wang, "Real-time faulted line localization and PMU placement in power systems through convolutional neural networks," *IEEE Trans. on Power Systems*, vol. 34, no. 6, pp. 4640–4651, Nov2019.

[64] A. Akrami, S. Asif, and H. Mohsenian-Rad, "Sparse distribution system state estimation: An approximate solution against low observability," in *Proc. of the IEEE PES Conference on Innovative Smart Grid Technologies (ISGT)*, Feb 2020.

[65] A. S. Zamzam and N. D. Sidiropoulos, "Physics-aware neural networks for distribution system state estimation," *IEEE Trans. on Power Systems*, vol. 35, no. 6, pp. 4347–4356, Nov 2020.

[66] M. Ghasemi Damavandi, V. Krishnamurthy, and J. Martí, "Robust meter placement for state estimation in active distribution systems," *IEEE Trans. on Smart Grid*, vol. 6, no. 4, pp. 1972–1982, Jul 2015.

[67] O. Wing, *Classical Circuit Theory*. Springer, New York, 2008.

[68] M. Farajollahi, A. Shahsavari, E. M. Stewart, and H. Mohsenian-Rad, "Locating the source of events in power distribution systems using micro-PMU data," *IEEE Transactions on Power Systems*, vol. 33, no. 6, pp. 6343–6354, May 2018.

[69] *https://site.ieee.org/pes-testfeeders/resources*.

[70] S. Das and B. K. Panigrahi, "A PMU-based data-driven approach for enhancing situational awareness in building a resilient power systems," *IEEE Trans. on Smart Grid*, vol. 18, no. 7, pp. 4773–4784, 2022.

[71] A. Shahsavari, M. Farajollahi, E. Stewart, E. Cortez, and H. Mohsenian-Rad, "Situational awareness in distribution grid using micro-PMU data: A machine learning approach," *IEEE Trans. on Smart Grid*, vol. 10, pp. 6167–6177, Nov. 2019.

[72] A. Akrami and H. Mohsenian-Rad, "Event-triggered distribution system state estimation: Sparse kalman filtering with reinforced coupling," *IEEE Trans. on Smart Grid*, vol. 15, no. 1, pp. 627–640, Jan 2024.

[73] B. Cui, A. K. Srivastava, and P. Banerjee, "Synchrophasor-based condition monitoring of instrument transformers using clustering approach," *IEEE Trans. on Smart Grid*, vol. 11, no. 3, pp. 2688–2698, 2020.

[74] B. Li, H. Li, W. He, B. Wei, S. Chen, and C. Yu, "Application of improved on-line monitoring method using pmu data in recent european blackout," in *2016 International Conference on Condition Monitoring and Diagnosis (CMD)*, Sep 2016.

[75] C. Lackner, J. H. Chow, and F. Wilches-Bernal, "Performance evaluation of statcom equipment using ambient and disturbance data," in *2019 IEEE Milan PowerTech, Milan, Italy*, Aug 2019.

[76] M. Kamal, M. Farajollahi, H. Nazaripouya, and H. Mohsenian-Rad, "Cyberattacks against event-based analysis in micro-PMUs: Attack models and counter measures," *IEEE Trans. on Smart Grid*, vol. 12, pp. 1577–1588, Mar. 2021.

[77] S. Bu, L. G. Meegahapola, D. P. Wadduwage, and A. M. Foley, "Stability and dynamics of active distribution networks (ADNs) with D-PMU technology: A review," *IEEE Trans. on Power Systems*, vol. 38, no. 3, pp. 2791–2804, 2023.

[78] S. Siamak, M. Dehghani, and M. Mohammadi, "Dynamic gps spoofing attack detection, localization, and measurement correction exploiting pmu and scada," *IEEE Systems Journal*, vol. 15, no. 2, pp. 2531–2540, 2021.

[79] C. Narduzzi, M. Bertocco, G. Frigo, and G. Giorgi, "Fast-TFM—multifrequency phasor measurement for distribution networks," *IEEE Trans. on Instrumentation and Measurement*, vol. 67, no. 8, pp. 1825–1835, Aug 2018.

[80] S. Jain, P. Jain, and S. N. Singh, "A fast harmonic phasor measurement method for smart grid applications," *IEEE Trans. on Smart Grid*, vol. 8, no. 1, pp. 493–502, Jan 2017.

[81] A. Vosughi, S. Pannala, and A. K. Srivastava, "Event detection, classification and localization in an active distribution grid using data-driven system identification, weighted voting and graph," *IEEE Trans. on Smart Grid*, vol. 14, no. 3, pp. 1843–1854, 2023.

[82] F. L. Grando, A. E. Lazzaretti, and M. Moreto, "The impact of PMU data precision and accuracy on event classification in distribution systems," *IEEE Trans. on Smart Grid*, vol. 13, no. 2, pp. 1372–1382, 2022.

[83] A. Aligholian, A. Shahsavari, E. M. Stewart, E. Cortez, and H. Mohsenian-Rad, "Unsupervised event detection, clustering, and use case exposition in micro-PMU measurements," *IEEE Trans. on Smart Grid*, vol. 12, no. 4, pp. 3624–3636, 2021.

[84] L. Bernard, S. Goondram, B. Bahrani, A. A. Pantelous, and R. Razzaghi, "Harmonic and interharmonic phasor estimation using matrix pencil method for phasor measurement units," *IEEE Sensors Journal*, vol. 21, pp. 945–954, 2020.

[85] F. Ahmadi-Gorjayi and H. Mohsenian-Rad, "A physics-aware MIQP approach to harmonic state estimation in low-observable power distribution systems using harmonic phasor measurement units," *IEEE Trans. on Smart Grid*, vol. 14, pp. 2111–2124, May 2022.

[86] C. Ge, R. A. de Oliveira, I. Y. H. Gu, and M. H. Bollen, "Deep feature clustering for seeking patterns in daily harmonic variations," *IEEE Trans. on Instrumentation and Measurement*, vol. 70, pp. 1–10, Aug 2020.

[87] B. Mallikarjuna, G. Pathirikkat, D. Sinha Roy, and J. B. R. Maddikara, "A real-time synchronized harmonic phasor measurements-based fault location method for transmission lines," *Journal of Control, Automation and Electrical Systems*, vol. 30, pp. 1082–1093, Jul 2019.

[88] B. Mallikarjuna, G. Pathirikkat, D. S. Roy, and J. B. R. Maddikara, "A real-time synchronized harmonic phasor measurements-based fault location method for transmission lines," *Journal of Control, Automation and Electrical Systems*, vol. 30, pp. 1082–1093, 2019.

[89] L. Chen, X. Xie, J. He, T. Xu, D. Xu, and N. Ma, "Wideband oscillation monitoring in power systems with high-penetration of renewable energy sources and power electronics: A review," *Renewable and Sustainable Energy Reviews*, vol. 175, p. 113148, Apr 2023.

[90] K. W. Louie, P. Wolson, R. A. Rivas, A. Wang, and P. Buchanan, "Discussion on power system harmonic analysis in the frequency domain," in *Proc. IEEE PES T & D Conference and Exposition*, jul 2006.

[91] A. Aligholian and H. Mohsenian-Rad, "GraphPMU: Event clustering via graph representation learning using locationally-scarce distribution-level fundamental and harmonic PMU measurements," *IEEE Trans. on Smart Grid*, vol. 14, no. 4, pp. 2960–2972, Jul 2023.

[92] M. Thomas and A. T. Joy, *Elements of Information Theory (Wiley Series in Telecommunications and Signal Processing)*. USA: Wiley, 2006.

[93] S. Ali, K. Wu, K. Weston, and D. Marinakis, "A machine learning approach to meter placement for power quality estimation in smart grid," *IEEE Trans. on Smart Grid*, vol. 7, no. 3, pp. 1552–1561, May 2016.

[94] Z. M. Wang, S. Y. Hu, and H. Song, "Channel selection method for eeg emotion recognition using normalized mutual information," *IEEE Access*, vol. 7, pp. 143 303–143 311, 2019.

[95] A. Punhani, N. Faujdar, K. K. Mishra, and M. Subramanian, "Binning-based silhouette approach to find the optimal cluster using k-means," *IEEE Access*, vol. 10, pp. 115 025–115 032, 2022.

[96] A. Silverstein and J. Follum, "High-resolution time-synchronized grid monitoring devices," North American Synchrophasor Initiative Technical Report NASPI-2020-TR-004, Mar. 2020.

[97] North American Electric Reliability Corporation, "Multiple Solar PV Disturbances in CAISO," NERC Report, Apr. 2022.

[98] L. Fan, Z. Miao, S. Shah, P. Koralewicz, V.Gevorgian, and J. Fu, "Data-driven dynamic modeling in power systems: A fresh look on inverter-based resource modeling," *IEEE Power & Energy Magazine*, Jun 2022.

[99] M. Abido and M. Khalid, "Seven-parameter PV model estimation using differential evolution," *Electrical Eng.*, vol. 100, pp. 971–981, 2018.

[100] P. P. Dash and M. kazerani, "Dynamic modeling and performance analysis of a grid-connected current-source inverter-based photovoltaic system," *IEEE Trans. on Sustainable Energy*, vol. 2, pp. 443–450, 2011.

[101] M. Ghazavi Dozein, B. C. Pal, and P. Mancarella, "Dynamics of inverter-based resources in weak distribution grids," *IEEE Trans. on Power Systems*, vol. 37, pp. 3682–3692, Jan 2022.

[102] P. Khaledian, A. Shahsavari, and H. Mohsenian-Rad, "Event-based dynamic response modeling of large behind-the-meter solar farms: A data-driven method based on real-world data," in *Proc. of the IEEE PES ISGT*, Washington, DC, Jan 2023.

[103] H. Mohsenian-Rad and W. Xu, "Synchro-waveforms: A window to the future of power systems data analytics," *IEEE Power and Energy Magazine 21*, vol. 21, no. 5, pp. 68–77, Sep 2023.

[104] D. C. Montgomery, C. L. Jennings, and M. Kulahci, *Introduction to Time Series Analysis and Forecasting.* John Wiley Sons, 2015.

[105] F. Ahmadi-Gorjayi, L. Lampe, and H. Mohsenian-Rad, "Event signatures in h-pmu measurements: An information-theoretic analysis of real-world data," in *Proc. of the IEEE PES ISGT*, Washington, DC, Feb 2024.

[106] F. Ahmadi-Gorjayi and H. Mohsenian-Rad, "Data-driven models for sub-cycle dynamic response of inverter-based resources using wmu measurements," *IEEE Trans. on Smart Grid*, vol. 14, pp. 4125–4128, 2023.

[107] D. Montenegro, R. Dugan, and G. Ramos, "Harmonics analysis using sequential-time simulation for addressing smart grid challenges," in *Proc. of 23rd Int. Conf. Electricity Distribution*, Lyon, France, Jun 2015.